Article

Auxiliary Reference Samples for Extrapolating Spectral Reflectance from Camera RGB Signals

Yu-Che Wen [1] , **Senfar Wen** [2,*] , **Long Hsu** [1] **and Sien Chi** [3]

1 Department of Electrophysics, National Yang Ming Chiao Tung University, No. 1001 University Road, Hsinchu 300, Taiwan; adam0682009.ep06g@nctu.edu.tw (Y.-C.W.); long@nctu.edu.tw (L.H.)
2 Department of Electrical Engineering, Yuan Ze University, No. 135 Yuan-Tung Road, Taoyuan 320, Taiwan
3 Department of Photonics, National Yang Ming Chiao Tung University, No. 1001 University Road, Hsinchu 300, Taiwan; schi@mail.nctu.edu.tw
* Correspondence: swen@saturn.yzu.edu.tw

Abstract: Surface spectral reflectance is useful for color reproduction. In this study, the reconstruction of spectral reflectance using a conventional camera was investigated. The spectrum reconstruction error could be reduced by interpolating camera RGB signals, in contrast to methods based on basis spectra, such as principal component analysis (PCA). The disadvantage of the interpolation method is that it cannot interpolate samples outside the convex hull of reference samples in the RGB signal space. An interpolation method utilizing auxiliary reference samples (ARSs) to extrapolate the outside samples is proposed in this paper. The ARSs were created using reference samples and color filters. The convex hull of the reference samples and ARSs was expanded to enclose outside samples for extrapolation. A commercially available camera was taken as an example. The results show that with the proposed method, the extrapolation error was smaller than that of the computationally time-consuming weighted PCA method. A low cost and fast detection speed for spectral reflectance recovery can be achieved using a conventional camera.

Keywords: spectrum reconstruction; spectral reflectance recovery; linear interpolation; principal component analysis

1. Introduction

Surface spectral reflectance is useful for the color reproduction of industrial products and artwork [1–3]. It can be measured directly with an imaging spectrometer [4,5]. However, direct spectral measurements are expensive. Indirect measurements using the spectrum reconstruction technique are of interest [6–14]. The spectrum of the image pixel is reconstructed from the channel outputs of the image acquisition device. Since no diffractive optical imaging system is required, the indirect method has the advantages of a low cost and fast detection speed. Therefore, using a conventional camera makes more field applications possible, e.g., smartphone cameras used as sensors to measure surface spectral reflectance.

Orthogonal projection [6], principal component analysis (PCA) [7,8], Gaussian mixture [9], non-negative matrix transformation (NMT) [10,11] and interpolation [11–14] have been proposed for spectrum reconstruction. Indirect methods that require training spectra are also known as learning-based methods, such as orthogonal projection, PCA and NMT. The training spectra are used to derive basis spectra. The reconstructed spectrum is a linear combination of basis spectra. The coefficients of basis spectra can be solved from simultaneous equations describing the channel outputs of the imaging device. The accuracy of the reconstructed spectrum increases with the number of channels. For cases with a conventional tricolor camera, where only three channels are available, the accuracy of the reconstructed spectrum might not be high enough.

The interpolation method uses reference spectra to reconstruct a spectrum interpolated from input values, e.g., XYZ tristimulus values [11–13] and RGB signal values [14]. Due

to the use of a look-up table (LUT) to store the reference spectra, this method is often referred to as the LUT method. The authors of [11–14] showed that the LUT method has the advantage of being more accurate than the PCA method, where the reference spectra for interpolation are the same as the training spectra for the PCA method. A spectrum is interpolated from its neighboring reference samples using the LUT method, whereas the basis spectra of the PCA method are derived from all training samples. The weighted PCA (wPCA) method was proposed to enhance the contribution of neighboring training samples in the CIELAB color space to the basis spectra [8,14]. Since basis spectra depend on the sample to be reconstructed, the computation time of the wPCA method is significantly increased compared to the conventional PCA method and the LUT method.

Learning-based methods require camera spectral sensitivities to formulate simultaneous equations describing the channel outputs. Camera spectral sensitivities can be directly measured using a monochromator [15], but accurate measurement is expensive. Without the use of a monochromator, the camera spectral sensitivities can be estimated by solving a quadric minimization problem [15,16]. An alternative approach is to estimate the spectral sensitivities including the camera and light source so that the reflectance spectrum can be calculated from the camera signals [17–21]. The estimation errors of spectral sensitivities cause additional errors in the reconstructed spectrum.

The LUT method does not require the spectral sensitivity functions because the reconstructed spectrum is interpolated from the measured spectra of the reference samples. However, if the sample lies outside the convex hull of the reference samples in the RGB signal space, it cannot be interpolated. Such a sample can be called an outside sample to distinguish it from the samples inside the convex hull. In the literature, modified PCA and NMT methods have been used to extrapolate outside samples [11–14], although spectral sensitivity functions are required. The authors of [11–13] considered interpolation in the XYZ color space, where spectral sensitivity functions were equivalently assumed to be the CIE color matching functions (CMFs). The authors of [14] considered interpolation in the RGB signal space, where the camera was assumed to follow the sRGB standard so that RGB signal values and XYZ tristimulus values can be converted to each other via the well-known sRGB matrix. This hypothetical camera is called the sRGB camera, and its spectral sensitivities are presented in [22].

The authors of [11,13] used 2D interpolation and 3D interpolation to extrapolate outside samples from reference samples, respectively. It is not guaranteed that the 2D interpolation method will extrapolate all outside samples [11]. The authors of [14] extrapolated outside samples from reference samples and additional reference samples; the latter are called model-based metameric spectra of extreme points (MMSEPs). The extreme points are the eight corners of the RGB signal cube. They are black, white, red, green, blue, yellow, cyan and magenta, corresponding to the signal vectors $[R, G, B]^T = [0, 0, 0]^T$, $[1, 1, 1]^T$, $[1, 0, 0]^T$, $[0, 1, 0]^T$, $[0, 0, 1]^T$, $[1, 1, 0]^T$, $[0, 1, 1]^T$ and $[1, 0, 1]^T$, respectively, where the maximum values of the signals are normalized to 1.0; the subscript T denotes the transpose operation. The metameric spectra are the reflection spectra from eight surfaces under D65 illumination. The spectral reflectance of the eight surfaces was constructed using the sRGB camera. The MMSEPs were equivalently constructed using the spectral sensitivities of the sRGB camera.

Inspired by [14], we propose the use of auxiliary reference samples (ARSs) for extrapolating outside samples using the LUT method. ARSs are high-saturation samples. They are created using appropriately chosen color filters and color chips. Color filters are in turn mounted on the spectroradiometer to measure the spectrum of filtered reflection light from a color chip. The RGB signal values corresponding to the filtered reflection light are recorded by a camera mounted with the same color filter. Color filters and color chips are chosen so that outside samples can be enclosed by reference samples and ARSs in the RGB signal space for extrapolation. Numerical studies of the proposed method were carried out. A comparison of the LUT method utilizing ARSs, the LUT method utilizing MMSEP

samples, the wPCA method and other methods is presented. For ease of reference, Table 1 lists the abbreviations defined herein in alphabetical order.

Table 1. Abbreviation list.

Abbreviation	Definition
ARS	Auxiliary Reference Sample
BSLB	Blue-Shift Lower Bound
CMF	Color Matching Function
FWHM	Full Width at Half Maximum
GFC	Goodness-of-Fit Coefficient
LUT	Look-Up Table
MAX	Maximum
MIN	Minimum
MMSEP	Model-based Metameric Spectra of Extreme Point
NMT	Non-negative Matrix Transformation
NTCC	Nearest Tetrahedron based on Circumcenter
NTCE	Nearest Tetrahedron based on Centroid
NTIC	Nearest Tetrahedron based on In-Center
PC50	50th Percentile
PC98	98th Percentile
PCA	Principal Component Analysis
RGF99	Ratio of Good Fit. (The ratio of samples with *GFC* > 0.99.)
RMS	Root Mean Square
RPRM	Root Polynomial Regression Model
SCI	Spectral Comparison Index
wPCA	Weighted Principal Component Analysis

2. Materials and Assessment Metrics

A Nikon D5100 camera was taken as an example. Its spectral sensitivities of the red, green and blue signal channels measured by a monochromator are shown in Figure 1a [16]. The average wavelengths of the spectral sensitivities of the red, green and blue channels are denoted as λ_{CamR}, λ_{CamG} and λ_{CamB}, respectively, which are called the channel wavelengths for simplicity. The full width at half maximum (FWHM) of the spectral sensitivities of the red, green and blue channels is denoted as $\Delta\lambda_{CamR}$, $\Delta\lambda_{CamG}$ and $\Delta\lambda_{CamB}$, respectively. The spectral specifications of the camera are shown in Table 2.
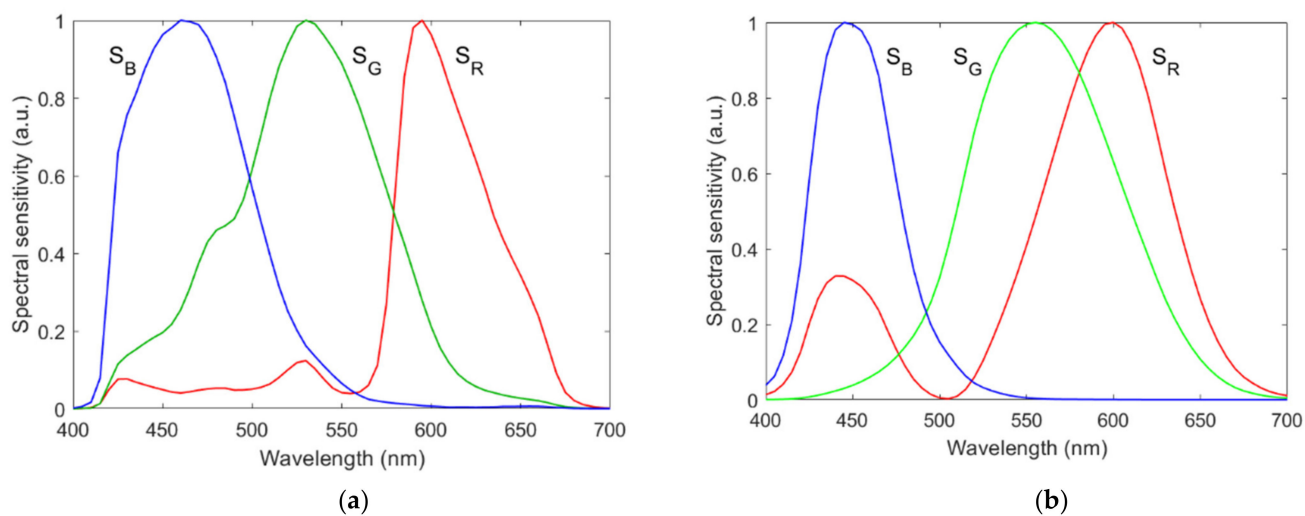

(**a**)　　　　　　　　　　　　　　(**b**)

Figure 1. Spectral sensitivities of (**a**) the Nikon D5100 and (**b**) the CMF camera. Spectral sensitivities of the red, green and blue signal channels are denoted as $\mathbf{S}_R$, $\mathbf{S}_G$ and $\mathbf{S}_B$, respectively.

Table 2. Spectral specifications of the Nikon D5100 and CMF cameras.

Specification	Channel Wavelength (nm)			FWHM Spectral Width (nm)		
Channel	B (λ_{CamB})	G (λ_{CamG})	R (λ_{CamR})	B ($\Delta\lambda_{\text{CamB}}$)	G ($\Delta\lambda_{\text{CamG}}$)	R ($\Delta\lambda_{\text{CamR}}$)
D5100	466.7	530.7	603.4	80.1	88.3	55.8
CMF	452.2	559.2	588.1	55.2	100.4	79.4

The reflectance spectra of matt Munsell color chips measured by a Perkin-Elmer lambda 9 spectroradiometer were adopted for preparing reference samples and test samples [23]. The available measurement data in [23] comprise 1269 records, but 2 of them are duplicates, namely, record 1242 (annotation 10RP 7/2) and record 1249 (annotation 10RP 7/4). Therefore, 1268 reflectance spectra were used in this paper. The light source was assumed to be illuminant D65. A total of 202 color chips were selected for the preparation of the reference samples.

A spectrum can be represented by the vector $S = [S(\lambda_1), S(\lambda_2), \ldots, S(\lambda_{Mw})]^T$, where $S(\lambda_j)$ is the spectral amplitude at wavelength λ_j, $\lambda_j = \lambda_1 + (j-1)\Delta\lambda$ is the j-th sampling wavelength, $j = 1, 2, \ldots, M_w$, and $\Delta\lambda$ is the wavelength sampling interval; M_w is the number of sampling wavelengths. In this paper, spectra were sampled from 400 nm to 700 nm in steps of 10 nm, i.e., $\lambda_1 = 400$ nm, $\Delta\lambda = 10$ nm and $M_w = 31$. The spectrum vector of the light reflected from a color chip is $S_{\text{Reflection}} = S_{\text{Ref}} \circ S_{\text{D65}}$, where S_{Ref} and S_{D65} are the spectral reflectance vector of the color chip and the spectrum vector of the illuminant D65, respectively; the operator $\circ$ is the Hadamard product, also known as the element-wise product. Figure 2a shows the color points of the reflection light from the 1268 Munsell color chips in the CIELAB color space, where the 202 reference samples and 1066 test samples are shown as red and blue dots, respectively. Figure 2b–d are the same as Figure 2a, but with different viewing angles. The CIE 1931 CMFs were adopted in this paper.
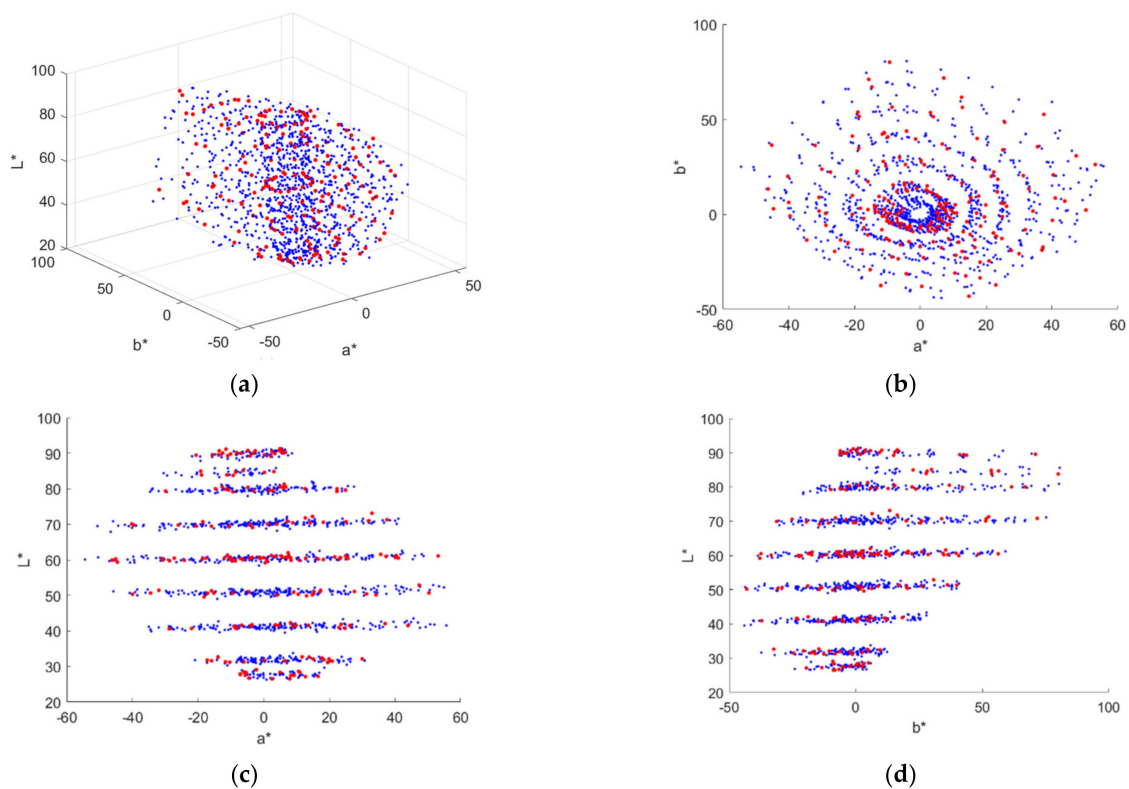

(a)

(b)

(c)

(d)

Figure 2. (**a**) Color points of the reflection light from Munsell color chips in CIELAB. (**b–d**) show the color points projected on the a*b* plane, a*L* plane and b*L* plane, respectively. Reference samples and test samples are shown as red and blue dots, respectively. The illuminant is D65.

The measured signal of a color channel is $U_{\text{Meas}} = S_{\text{Reflection}}^{\text{T}} S_{\text{U}}$, where $U = R$, G and B for the red, green and blue channels, respectively; $S_{\text{Reflection}}$ is the reflection spectrum vector; S_{U} is the spectral sensitivity of the channel. For the white balance condition, the channel signals are normalized to $U = U_{\text{Meas}}/U_{\text{MeasD65}}$, where $U = R$, G and B; U_{MeasD65} is the measured signal when $S_{\text{Reflection}} = S_{\text{White}} \circ S_{\text{D65}}$; S_{White} is the spectral reflectance of a white card. The white side of a Kodak gray card was taken as the white card, where its spectral reflectance is approximately 0.9 in the visible wavelength range. The vector representing the camera signals is designated as $C = [R, G, B]^{\text{T}}$. Figure 3a shows the color points of the reflection spectra from the Munsell color chips in the RGB signal space using the Nikon D5100, where the 202 reference samples and 1066 test samples are shown as red and blue dots, respectively. There are 62 samples in the convex hull of the 202 reference samples. Figure 3b shows the convex hull.
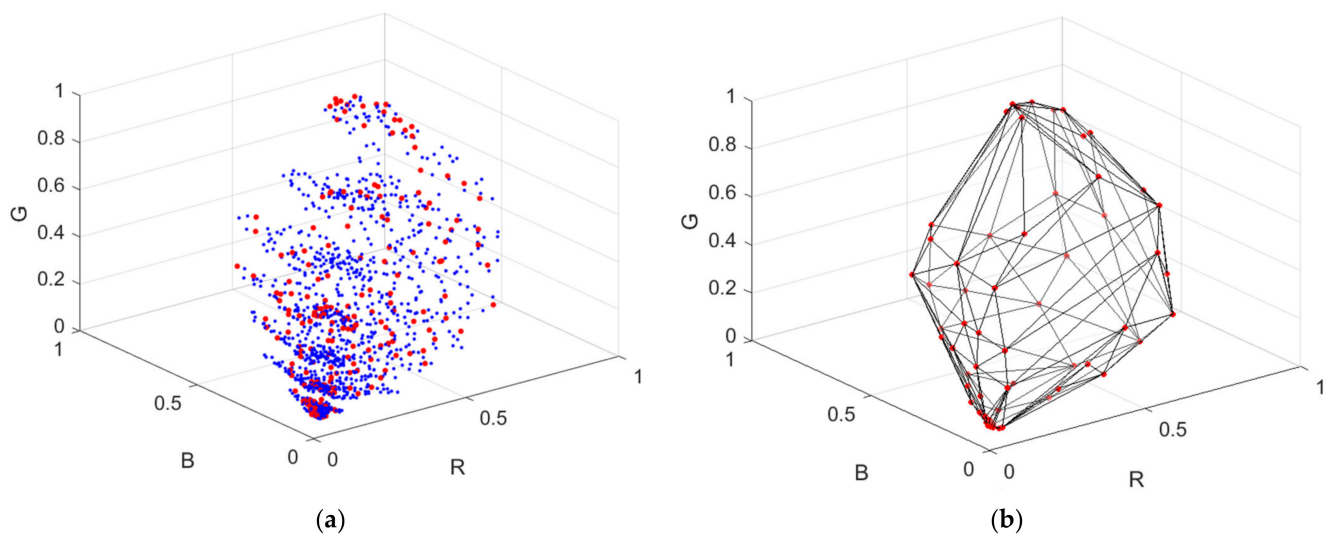

(a) (b)

Figure 3. (**a**) Color points of the reflection light from Munsell color chips in the RGB signal space using the Nikon D5100, where reference samples and test samples are shown as red and blue dots, respectively. The illuminant is D65. (**b**) Convex hull of reference samples H_{R}.

For a given test signal vector, the LUT method to reconstruct the reflection light spectrum is shown in Section 3.1. The reconstructed spectrum vector is designated as S_{Rec}. The reconstructed spectral reflectance vector S_{RefRec} was calculated as the reflection spectrum vector S_{Rec} divided by the D65 spectrum vector S_{D65} element by element.

The reconstructed spectral reflectance vector S_{RefRec} was assessed by the root mean square (RMS) error $E_{\text{Ref}} = (|S_{\text{RefRec}} - S_{\text{Ref}}|^2/M_{\text{w}})^{1/2}$ and the goodness-of-fit coefficient $GFC = |S_{\text{RefRec}}^{\text{T}} S_{\text{Ref}}| / |S_{\text{RefRec}}| |S_{\text{Ref}}|$, where $|\cdot|$ stands for the norm operation. The color difference between S_{Rec} and $S_{\text{Reflection}}$ was assessed using CIEDE2000 ΔE_{00}. The spectral comparison index (*SCI*) was also used to assess the reconstructed results [24,25]. The parameter k in the formula for calculating *SCI* shown in [24] was set to 1.0. For the values of E_{Ref}, ΔE_{00} and *SCI*, the smaller, the better. The statistics of the three metrics were calculated, which are the mean μ, standard deviation σ, 50th percentile *PC50*, 98th percentile *PC98* and maximum *MAX*. For the value of *GFC*, the larger, the better. The statistics of *GFC* were calculated, which are the mean μ, standard deviation σ, 50th percentile *PC50* and minimum *MIN*. The fit of the spectral curve shape is good if *GFC* > 0.99 [14,26]. The ratio of samples with *GFC* > 0.99 was calculated, which is called the ratio of good fit and designated as *RGF99*.

3. Spectrum Reconstruction Method

3.1. Reflection Spectrum Reconstruction

This subsection describes the LUT method to reconstruct the reflection spectrum vector S_{Rec} from the test signal vector C [12]. The color points of the reference samples in the RGB signal space were not regularly distributed as shown in Figure 3a. Therefore, the use of the scattered data interpolation method was required. Several interpolation methods were surveyed in [27]. Among these methods, linear tetrahedral interpolation was adopted due to its simplicity and computational time savings [11–13]. A tetrahedral mesh in the RGB signal space was generated from the reference signal vectors. Note that the tetrahedrization is not unique, and the interpolation result depends on the tetrahedrization [12,27]. All programs in this paper were implemented in MATLAB (version R2021a, MathWorks). The tetrahedral mesh used for interpolation was generated by the MATLAB function "delaunay" [11,13,14]. There were three steps to interpolate the test sample.

STEP 1: Locate the tetrahedron.

The tetrahedron that encloses the color point Q of the vector C in the RGB signal space was located. Figure 4 shows the tetrahedron, with vertices Q_1, Q_2, Q_3 and Q_4 enclosing the color point Q. A database or look-up table storing the tetrahedral mesh can be used to save processing time in locating the tetrahedron [13]. This paper used the MATLAB function "pointLocation" to locate the tetrahedron, which is a related function of "delaunay".
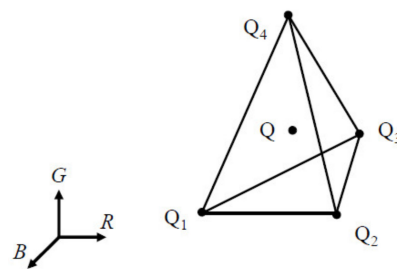

Figure 4. Schematic diagram showing a color point Q enclosed by a tetrahedron with vertices Q_1, Q_2, Q_3 and Q_4 in the RGB signal space.

STEP 2: Calculate interpolation coefficients.

The reference signal vectors of Q_1, Q_2, Q_3 and Q_4 were assumed to be C_1, C_2, C_3 and C_4, respectively. It is required that C is the linear combination of the reference signal vectors, and

$$C = \alpha_1 C_1 + \alpha_2 C_2 + \alpha_3 C_3 + \alpha_4 C_4, \tag{1a}$$

$$1 = \alpha_1 + \alpha_2 + \alpha_3 + \alpha_4, \tag{1b}$$

where the coefficients α_1, α_2, α_3 and α_4 are weighting factors. Equation (1a) comprises three scalar equations because tristimulus vectors are 3D. Equation (1b) guarantees that Q is inside the tetrahedron if $0 < \alpha_1, \alpha_2, \alpha_3, \alpha_4 < 1$. The four coefficients in Equation (1a,b) were solved.

STEP 3: Calculate the reconstructed reflection spectrum.

The reconstructed reflection spectrum vector is

$$S_{\text{Rec}} = \alpha_1 S_1 + \alpha_2 S_2 + \alpha_3 S_3 + \alpha_4 S_4, \tag{2}$$

where S_j is the reference spectrum vector corresponding to the vertex Q_j for j = 1, 2, 3 and 4. If the reconstructed spectrum has negative values, the value is set to zero.

If both sides of Equation (2) are multiplied by the spectral sensitivity function of a signal channel and integrated over the wavelength, we obtain Equation (1a) corresponding to the signal channel. However, the interpolation is an inverse problem. The reconstructed

spectrum vector S_{Rec} is one of numerous metameric spectrum vectors corresponding to the test signal vector C. Equation (1a,b) are the four constraints for finding a metameric spectrum vector. The difference between the target spectral reflectance vector S_{Ref} and the reconstructed spectral reflectance vector S_{RefRec} calculated from the metameric spectrum vector S_{Rec} was assessed using the metrics defined in Section 2.

3.2. Spectral Reflectance Reconstruction Workflow

Figure 5 shows a flow chart for reconstructing the spectral reflectance vector S_{RefRec} from the test signal vector C. The convex hull of the tetrahedral mesh of the reference signal vectors is denoted as H_R. An example of H_R is shown in Figure 3b. The convex hull of the tetrahedral mesh of the reference signal vectors and ARS vectors is denoted as H_{RA}. The method for creating ARSs is shown in Section 4.
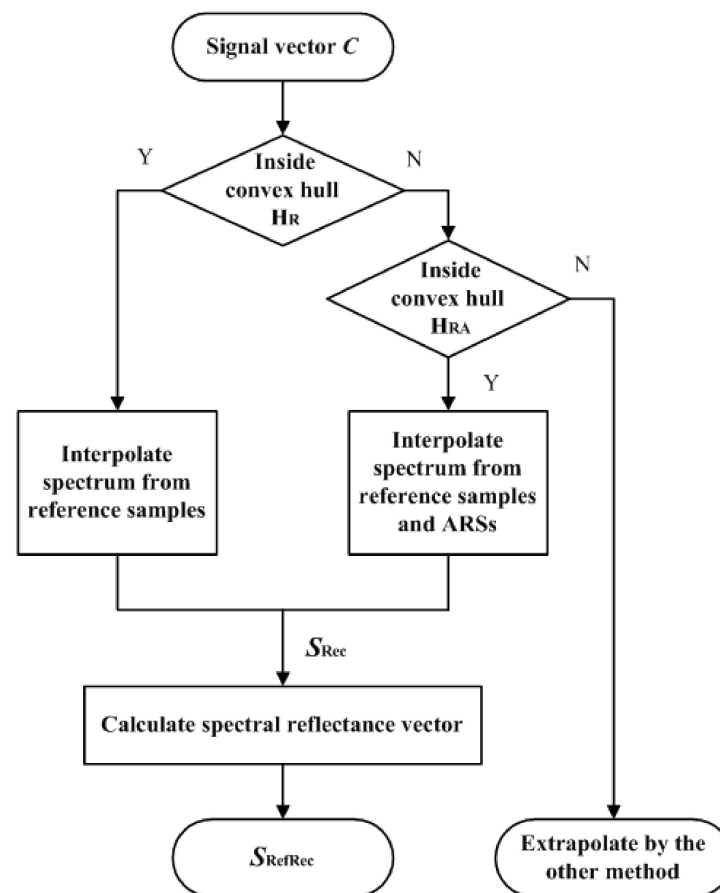

Figure 5. Flow chart for reconstructing the spectral reflectance vector S_{RefRec} from the signal vector C. Refer to Section 3.2 for details.

If the test signal vector is inside H_R, its reflection spectrum vector S_{Rec} is interpolated from the reference samples using the three-step procedure in Section 3.1. If the test signal vector is outside H_R and inside H_{RA}, its reflection spectrum vector S_{Rec} is extrapolated from the expanded reference sample set including the reference samples and ARSs using the three-step procedure in Section 3.1. If the test signal vector is outside H_{RA}, its reflection spectrum vector must be extrapolated using the other method. Therefore, ARSs must be chosen to guarantee that the test signal vectors of interest are inside H_{RA}.

4. Auxiliary Reference Samples

4.1. ARS Creation

The ARSs were described in the last paragraph of Section 1. Figure 6 shows a five-step flow chart for creating a set of ARSs. The description below uses the Nikon D5100 as an example. The example color filters were optimized for the Nikon D5100.
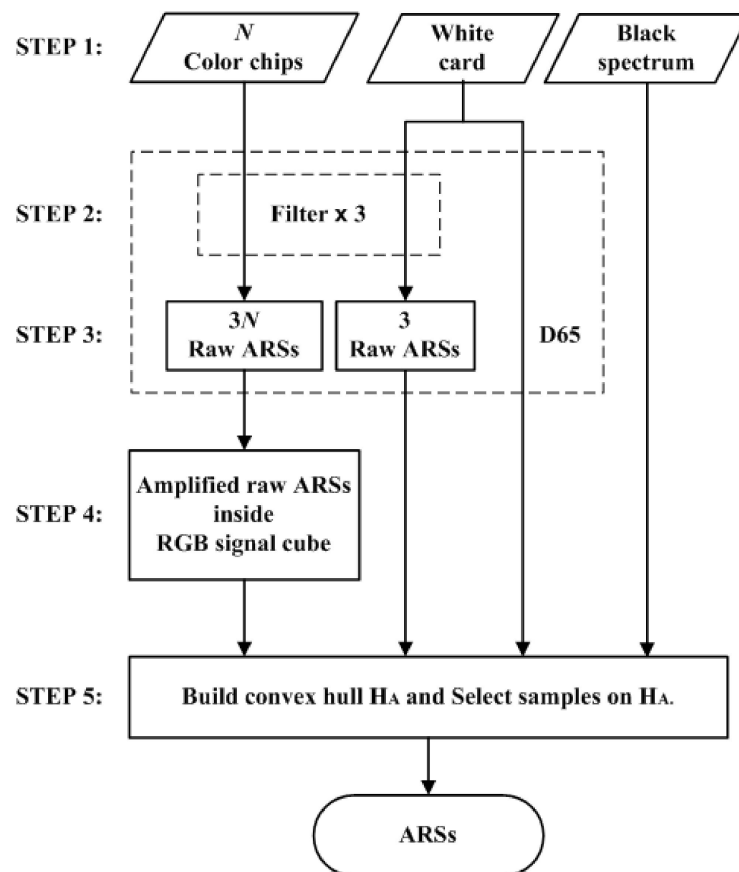

Figure 6. Flow chart for creating auxiliary reference samples (ARSs). Refer to Section 4.1 for details.

STEP 1: Select reflective surfaces.

The Munsell color chips in the convex hull in CIELAB and the white card were used as reflective surfaces to create ARSs. The number of color chips in the convex hull in Figure 2a is $N = 62$. The reference samples in the convex hull in Figure 3b are the reflection samples from the same 62 color chips. Samples of the white point and black point are default ARSs. The white ARS is the white point sample, whose signal vector is $[1, 1, 1]^T$. The illuminant is D65. The spectrum of the black ARS is zero, and its signal vector is $[0, 0, 0]^T$.

STEP 2: Select color filters.

Appropriate cyan, yellow and magenta filters were selected. They were used to filter reflection light to increase color saturation. Figure 7a shows the spectral transmittance of an example filter set. Given a reference sample of a signal vector $[R, G, B]^T$, its signal vector becomes $[R_f, G_f, B_f]^T$ after filtering. If the filter is cyan, the ratios B_f/R_f and G_f/R_f will be larger than B/R and G/R, respectively, and a more saturated sample is created. If the reference sample is magenta ($G << B, R$), a highly saturated blue sample is created. The issue of color filter selection is discussed further in Section 4.2.
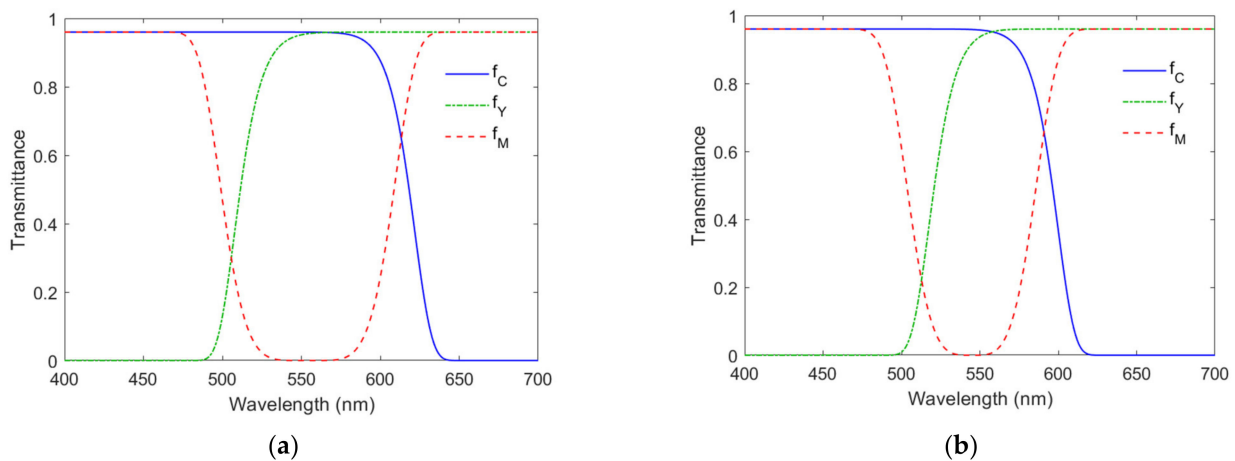
(**a**)　　　　　　　　　　　　　　　　　　　　　　　(**b**)

Figure 7. Spectral transmittance of the color filters optimized for (**a**) the Nikon D5100 and (**b**) the CMF camera. The spectral transmittance of the cyan, yellow and magenta filters is denoted as f_C, f_Y and f_M, respectively.

STEP 3: Measure raw ARSs.

　　　The color filters selected in STEP 2 were sequentially mounted on the camera and the spectroradiometer for measurement. For each color filter, the RGB signal values and spectrum of the reflection light from the reflective surfaces selected in STEP 1 were measured. There were $3N + 3 = 189$ measured samples using the color filters, called the raw ARSs. In this paper, the RGB signal values and spectra were calculated according to Section 2 for numerical study. Figure 8a shows an example of the raw ARSs in the RGB signal space, where the color filters in Figure 7a are used. In Figure 8a, the raw ARSs from the color chips and the white card are shown as red dots and crosses, respectively.

(**a**)　　　　　　　　　　　　　　　　　　　　　　　(**b**)
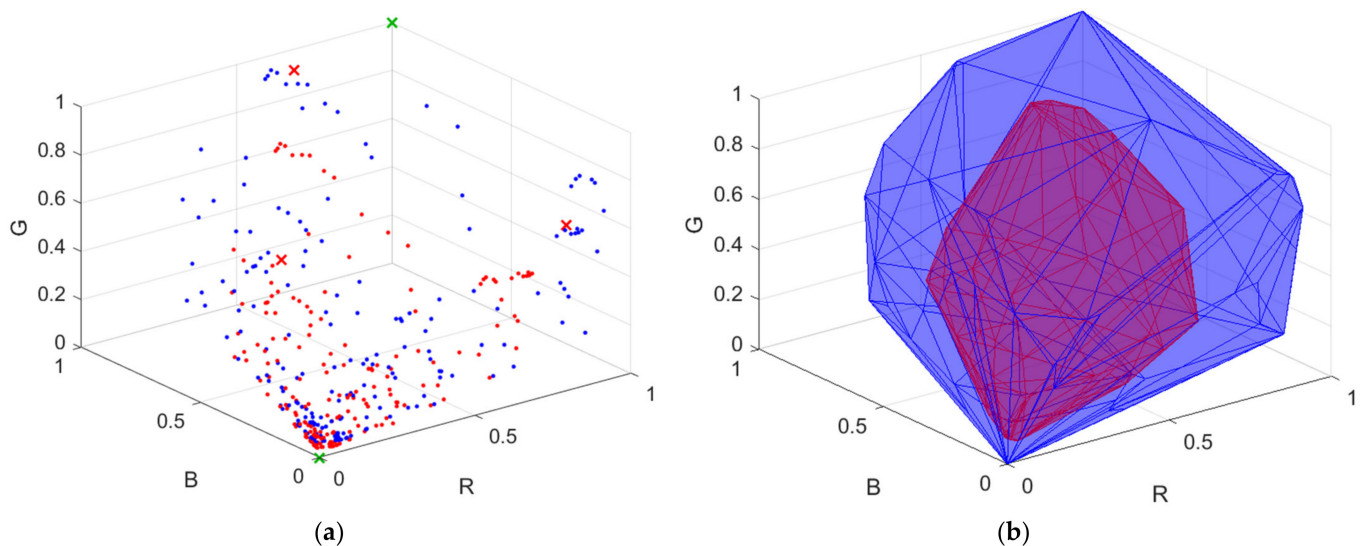
Figure 8. (**a**) Color points of raw ARSs and amplified raw ARSs shown as red and blue dots, respectively, in the RGB signal space. The raw ARSs from the white card are shown as red crosses. The white and black ARSs are shown as green crosses. Color filters optimized for the Nikon D5100 are used. (**b**) The convex hull H_A of the ARSs and the convex hull H_R of the reference samples are shown as blue and red meshes, respectively. Figure 3b shows the same H_R.

STEP 4: Create amplified raw ARSs.

　　　From Figures 3a and 8a, we can see that the $3N$ raw ARSs from the color chips cannot properly enclose the test samples due to attenuation of the reflection light passing through

the filter. The spectra and RGB signal vectors of these raw ARSs were multiplied by an amplification factor γ greater than 1.0. If an RGB signal vector is multiplied by an amplification factor, its color point in the RGB signal space moves away from the black point in the direction from the black point to its original color point. The value of γ could be sample-dependent to reduce extrapolation error. For simplicity, $\gamma = 1.5$ was empirically set for all these samples except for the samples corresponding to the color chips of L* = 90 in Figure 2a–d, which have a value of 9 in the Munsell annotation. The exception samples were multiplied by a smaller amplification factor so that they remained within the RGB signal cube, where $\gamma = 1.185$. All amplified raw ARSs are shown as blue dots in Figure 8a.

STEP 5: Select the ARSs.

The ARSs are the samples in the convex hull of the amplified raw ARSs, the three raw ARSs from the white card, the white ARS and the black ARS. The latter two are shown as green crosses in Figure 8a. The convex hull is denoted as H_A and is shown as a blue mesh in Figure 8b. The total number of ARSs in H_A is 53. The convex hull of the reference samples H_R defined in Section 3.2 is also shown as a red mesh in Figure 8b for comparison. From Figure 8b, H_R is completely inside H_A. In this case, H_A and H_{RA} are the same because the color points of the reference samples are well enclosed by H_A. It seems unnecessary to measure 189 samples in STEP 3 as there are only 53 samples in H_A. However, before building H_A, we do not know which samples will be in H_A.

4.2. Color Filter Design Method

Only cyan, yellow and magenta filters were selected in STEP 2 and used in STEP 3. Extrapolation error can be further reduced by using more color filters, e.g., using additional red, green and blue filters. This paper limited the number of color filters to three because (1) the use of cyan, yellow and magenta color filters enables all outside samples to be extrapolated for the cases under consideration, and (2) the cost of creating ARSs increases with the number of color filters. The spectral transmittance functions of the considered cyan, yellow and magenta filters are based on a super-Gaussian function. Such color filters can be absorption filters or interference filters [28]. There are stock color filters in various specifications on the market.

The cyan filter is a short-pass optical filter whose spectral transmittance is assumed to be

$$f_C(\lambda) = f_{C0} \exp\left[-\left(\frac{\lambda - \lambda_S}{\sigma_C}\right)^{a_C}\right] \tag{3}$$

where f_{C0} is the maximum transmittance; $\lambda_S = 400$ nm; σ_C and a_C are parameters determined by the filter edge wavelength λ_C and edge width $\Delta\lambda_C$. Figure 9a shows the definitions of λ_C and $\Delta\lambda_C$. The edge wavelength λ_C is the wavelength of the half-maximum transmittance, i.e., $f_C(\lambda_C) = 0.5 f_{C0}$. The edge width $\Delta\lambda_C$ is the wavelength interval from $0.1 f_{Y0}$ to $0.9 f_{Y0}$. From Equation (3) and the definitions of λ_C and $\Delta\lambda_C$, the following equation can be derived.

$$\left[(\ln 10)^{\frac{1}{a_C}} - (-\ln 0.9)^{\frac{1}{a_C}}\right](\lambda_C - \lambda_S) = (\ln 2)^{\frac{1}{a_C}} \Delta\lambda_C, \tag{4}$$

Given the values of λ_C and $\Delta\lambda_C$, the value of a_C can be solved from Equation (4) using the MATLAB function "fzero". After the value of a_C is solved, the parameter σ_C can be easily calculated by

$$\sigma_C = (\ln 2)^{-\frac{1}{a_C}}(\lambda_C - \lambda_S) \tag{5}$$

The yellow filter is a long-pass color filter whose spectral transmittance is assumed to be

$$f_Y(\lambda) = f_{Y0} \exp\left[-\left(\frac{\lambda_L - \lambda}{\sigma_Y}\right)^{a_Y}\right] \tag{6}$$

where f_{Y0} is the maximum transmittance; $\lambda_L = 700$ nm; σ_Y and a_Y are parameters determined by the filter edge wavelength λ_Y and edge width $\Delta\lambda_Y$. Figure 9a also shows

the definitions of λ_Y and $\Delta\lambda_Y$, which are similar to those of λ_C and $\Delta\lambda_C$. The parameters σ_Y and a_Y can be solved from the same equations as Equations (4) and (5), except that a_C, $(\lambda_C - \lambda_S)$ and $\Delta\lambda_C$ in Equation (4) are replaced by a_Y, $(\lambda_L - \lambda_Y)$ and $\Delta\lambda_Y$, respectively, and σ_C, a_C and $(\lambda_C - \lambda_S)$ in Equation (5) are replaced by σ_Y, a_Y and $(\lambda_L - \lambda_Y)$, respectively.
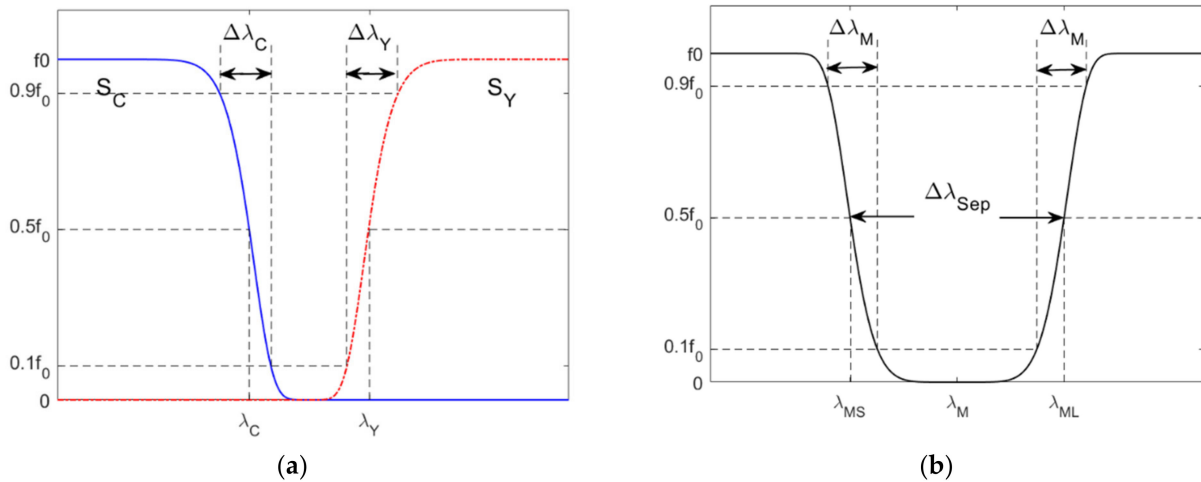

Figure 9. Schematic diagrams showing the specification definitions of the (**a**) cyan and yellow color filters, and (**b**) magenta filter. Refer to Section 4.2 for details.

The magenta filter is a notch optical filter whose spectral transmittance is assumed to be

$$f_M(\lambda) = f_{M0}\left(1 - \exp\left[-\left|\frac{\lambda - \lambda_M}{\sigma_M}\right|^{a_M}\right]\right) \tag{7}$$

where f_{M0} is the maximum transmittance; λ_M is the central wavelength; σ_M and a_M are parameters determined by the wavelength separation $\Delta\lambda_{Sep}$ and edge width $\Delta\lambda_M$. Figure 9b shows the definitions of $\Delta\lambda_{Sep}$ and $\Delta\lambda_M$. The wavelength separation $\Delta\lambda_{Sep} = \lambda_{ML} - \lambda_{MS}$, where λ_{ML} and λ_{MS} are the edge wavelengths at the long-wavelength side and the short-wavelength side of the filter spectral transmittance, respectively. The central wavelength $\lambda_M = (\lambda_{MS} + \lambda_{ML})/2$. The definition of the edge width $\Delta\lambda_M$ is similar to $\Delta\lambda_C$. From Equation (7) and the definitions of $\Delta\lambda_{Sep}$ and $\Delta\lambda_M$, the following equation can be derived:

$$\left[(\ln 10)^{\frac{1}{a_M}} - (-\ln 0.9)^{\frac{1}{a_M}}\right]\Delta\lambda_{Sep} = 2(\ln 2)^{\frac{1}{a_M}}\Delta\lambda_M. \tag{8}$$

Given the values of $\Delta\lambda_{Sep}$ and $\Delta\lambda_M$, the value of a_M can be solved from Equation (8). After the value of a_M is solved, the parameter σ_M can be easily calculated by

$$\sigma_M = 2(\ln 2)^{-\frac{1}{a_M}}\Delta\lambda_{Sep} \tag{9}$$

The wavelengths λ_{MS} and λ_{ML} were taken as the specifications of the magenta filter, where $\lambda_{MS} = \lambda_M - \Delta\lambda_{Sep}/2$ and $\lambda_{ML} = \lambda_M + \Delta\lambda_{Sep}/2$.

For simplicity, the maximum transmittance of the filters was set to 0.96, i.e., $f_{Y0} = f_{C0} = f_{M0} = 0.96$; all edge widths for the three filters were set to 30 nm, i.e., $\Delta\lambda_Y = \Delta\lambda_C = \Delta\lambda_M = 30$ nm. The four edge wavelengths λ_C, λ_Y, λ_{MS} and λ_{ML} were optimized for the minimum mean E_{Ref} of the outside samples under the constraints

$$\lambda_{CamG} \leq \lambda_C \leq \lambda_{CamR} + \Delta\lambda_{CamR}/2, \tag{10a}$$

$$\lambda_{CamB} \leq \lambda_Y \leq \lambda_{CamG} + \Delta\lambda_{CamG}/2, \tag{10b}$$

$$\lambda_{CamB} \leq \lambda_{MS} \leq \lambda_{CamG}, \tag{10c}$$

$$\lambda_{\text{CamG}} \leq \lambda_{ML} \leq \lambda_{\text{CamR}} + \Delta\lambda_{\text{CamR}}/2. \tag{10d}$$

The constraints are empirical, but reasonable. For example, from Equation (10a), the edge wavelength λ_C of the cyan filter should lie between the wavelengths of the green and red camera channels so that the spectrum amplitudes at short and medium wavelengths are less attenuated. Half the bandwidth of the spectral sensitivity was used as the tolerance for the upper bound in Equation (10a,b,d).

The optimization process consisted of two steps. The first step was to optimize the four edge wavelengths using the Bayesian optimization function "bayesopt" implemented in MATLAB. The objective function is the mean E_{Ref} of outside samples. Since Bayesian optimization does not use the derivative of the objective function to find the minimum objective value [29], the second step used the MATLAB optimization function "lsqnonlin" to further optimize the four edge wavelengths, where the result of the first step was taken as the initial trial solution. The function "lsqnonlin" was used because the optimization problem is nonlinear. The optimized edge wavelengths λ_C, λ_Y, λ_{MS} and λ_{ML} are denoted as λ_{Copt}, λ_{Yopt}, λ_{MSopt} and λ_{MLopt}, respectively.

The edge wavelengths of the optimized filters for the Nikon D5100 are shown in Table 3. The spectral transmittance of the optimized color filters is shown in Figure 7a. The convex hulls H_A and H_{RA} using the optimized filters are shown as blue meshes in Figures 8b and 10, respectively, though they are the same for the case considered.

Table 3. Edge wavelengths of the optimized color filters for the Nikon D5100 and CMF cameras.

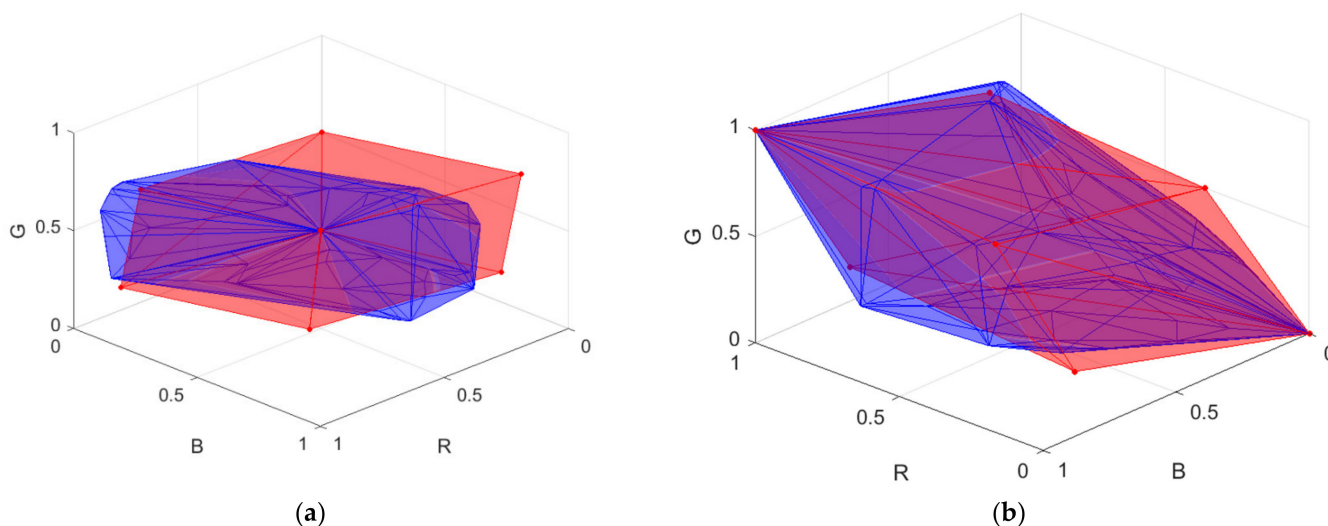|	λ_{Copt} (nm)	λ_{Yopt} (nm)	λ_{MSopt} (nm)	λ_{MLopt} (nm)
D5100	618.9	510.8	499.7	608.1
CMF	596.7	520.5	504.0	585.4

(a)

(b)

Figure 10. (**a**) The convex hull H_{RA} of the reference samples and ARSs and the convex hull of the MMSEP samples are shown as blue and red meshes, respectively. The ARSs are the same as in Figure 3b, where optimized color filters are used. The convex hull H_{RA} is the same as the convex hull H_A in Figure 8b, but the viewing angle is different. (**b**) is the same as (**a**), except it rotates 90° clockwise along the *G* axis.

5. Results and Discussion

In this section, in addition to the Nikon D5100, an artificial camera is used as a second camera for comparison. The spectral sensitivities of the artificial camera were assumed to be the CIE 1931 CMFs as shown in Figure 1b. It is called the CMF camera, whose spectral specifications are shown in Table 2. The camera used in the numerical results below is the Nikon D5100 unless otherwise specified.

5.1. Interpolation

Table 4 shows the assessment metric statistics for the test samples using the LUT method, where the Nikon D5100 and CMF cameras were used. As can be seen from Table 4, out of the 1066 test samples, about 860 samples were inside samples that can be interpolated. The table also shows the extrapolation results for about 200 outside samples, which are discussed in the next subsection. The assessment metric statistics for the inside samples using the two cameras were about the same except for the color difference ΔE_{00}. If the spectral sensitivities of a camera are different from the CMFs, the color difference ΔE_{00} will be a non-zero value from Equations (1a) and (2). While not zero, most of the inside samples using the Nikon D5100 showed little color difference.

Table 4. Assessment metric statistics for test samples using the LUT method and optimized color filters. The Nikon D5100 and CMF cameras were used.

	Camera	Nikon D5100			CMF		
Metric	**Sample**	**All**	**Inside**	**Outside**	**All**	**Inside**	**Outside**
	No.	**1066**	**864**	**202**	**1066**	**863**	**203**
E_{Ref}	mean μ	0.0129	0.0120	0.0171	0.0132	0.0123	0.0169
	std σ	0.0118	0.0107	0.0150	0.0116	0.0103	0.0152
	PC50	0.0091	0.0087	0.0132	0.0099	0.0094	0.0132
	PC98	0.0509	0.0485	0.0599	0.0494	0.0444	0.0650
	MAX	0.1078	0.0859	0.1078	0.1111	0.0816	0.1111
GFC	mean μ	0.9972	0.9974	0.9962	0.9972	0.9974	0.9960
	std σ	0.0074	0.0071	0.0084	0.0063	0.0054	0.0090
	PC50	0.9993	0.9994	0.9986	0.9993	0.9994	0.9986
	MIN	0.9000	0.9000	0.9193	0.9161	0.9457	0.9161
	RGF99	0.9353	0.9375	0.9257	0.9203	0.9212	0.9163
ΔE_{00}	mean μ	0.4244	0.4239	0.4262	0.0000	0.0000	0.0000
	std σ	0.4115	0.4182	0.3827	0.0000	0.0000	0.0000
	PC50	0.2823	0.2795	0.3015	0.0000	0.0000	0.0000
	PC98	1.6842	1.6900	1.6402	0.0000	0.0000	0.0000
	MAX	2.5918	2.5918	1.8962	0.0000	0.0000	0.0000
SCI	mean μ	4.1102	3.7503	5.6495	4.1869	3.8632	5.5631
	std σ	3.1802	2.9266	3.7252	3.0695	2.8885	3.4233
	PC50	3.1484	2.9310	4.6951	3.3348	3.1732	4.8976
	PC98	13.4611	12.1239	15.0412	12.4129	11.7579	14.3999
	MAX	25.2299	25.2299	21.9370	23.8934	23.8934	15.7186

The spectrum reconstructions of the test samples using the PCA and wPCA methods are considered for comparison. In the wPCA method, the *i*-th training sample was multiplied by a weighting factor $1/(\Delta E_i + s)$, where ΔE_i is the color difference between the test sample and the *i*-th training sample in CIELAB; s is a small-valued constant to avoid division by zero [8]. Weighted training samples were used to derive basis spectra. A camera device model was used to convert RGB signal values into tristimulus values for calculating ΔE_i. A third-order root polynomial regression model (RPRM) was employed and trained using the reference samples [30]. The accuracy of the RPRM was slightly higher than that of the polynomial regression model in this case.

The PCA and wPCA methods were used to reconstruct all test samples using the spectral sensitivities of the Nikon D5100 in Figure 1a. Table 5 shows the assessment metric statistics for the test samples using the PCA and wPCA methods, where the inside samples and outside samples were the same as those using the LUT method. The spectrum reconstruction error using the wPCA method was apparently smaller than that using the PCA method, as expected. Comparing Table 4 with Table 5, we can see that the LUT method outperformed the wPCA method except for *GFC*. Figure 11a,b show the E_{Ref} and

GFC histograms for the 864 inside samples, respectively, where the cases using the LUT, PCA and wPCA methods are shown.

Table 5. Assessment metric statistics for test samples using the PCA and wPCA methods. The camera is the Nikon D5100.

| Metric	Method	PCA			wPCA		
	Sample	All	Inside	Outside	All	Inside	Outside
	No.	1066	864	202	1066	864	202
E_{Ref}	mean μ	0.0221	0.0193	0.0341	0.0147	0.0131	0.0213
	std σ	0.0168	0.0128	0.0247	0.0122	0.0092	0.0194
	PC50	0.0173	0.0160	0.0276	0.0121	0.0114	0.0155
	PC98	0.0817	0.0515	0.1152	0.0565	0.0402	0.0774
	MAX	0.1442	0.1180	0.1442	0.1255	0.0894	0.1255
GFC	mean μ	0.9940	0.9958	0.9860	0.9972	0.9982	0.9931
	std σ	0.0101	0.0072	0.0155	0.0062	0.0031	0.0118
	PC50	0.9974	0.9977	0.9892	0.9990	0.9990	0.9976
	MIN	0.8858	0.8982	0.8858	0.8921	0.9444	0.8921
	RGF99	0.8349	0.9178	0.4802	0.9418	0.9803	0.7772
ΔE_{00}	mean μ	0.8261	0.6970	1.3780	0.5017	0.4318	0.8011
	std σ	0.6202	0.4163	0.9572	0.4650	0.3099	0.7887
	PC50	0.7003	0.6488	1.1215	0.3793	0.3600	0.5094
	PC98	2.8667	1.7963	3.6855	2.2116	1.2505	3.0850
	MAX	4.3546	3.0765	4.3546	3.3029	2.3674	3.3029
SCI	mean μ	7.8531	6.3217	14.4032	4.7942	3.9033	8.6050
	std σ	6.5329	4.2839	9.7024	4.3745	2.7381	7.1555
	PC50	5.8291	5.0862	12.0428	3.4185	3.1503	6.3268
	PC98	27.2764	19.6718	38.8951	19.1506	11.8655	31.3431
	MAX	55.4331	27.4239	55.4331	35.2093	26.8467	35.2093
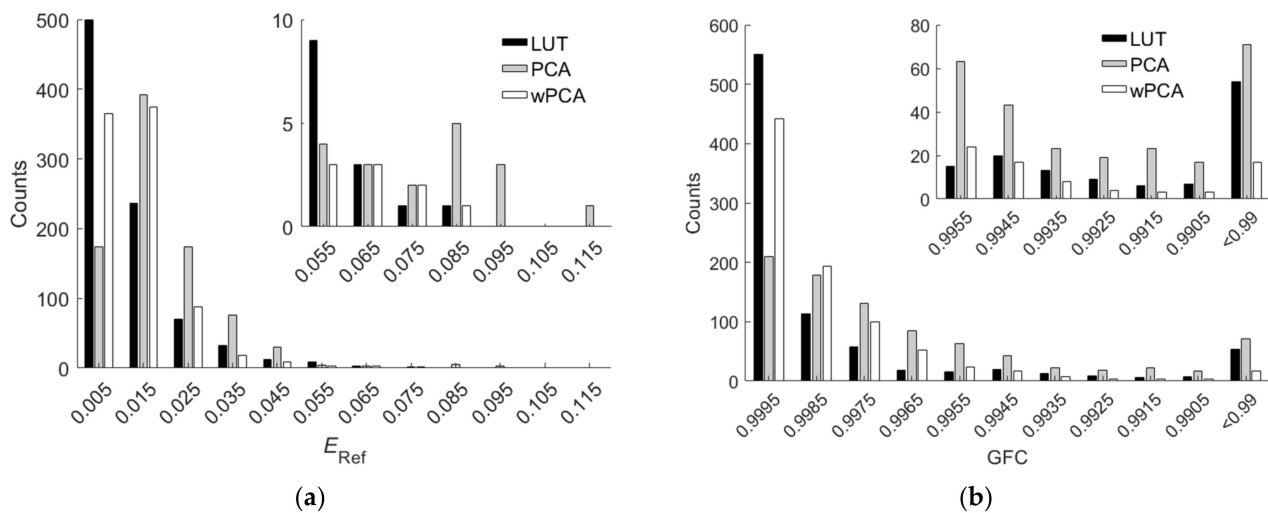
Figure 11. (**a**) E_{Ref} and (**b**) *GFC* histograms for the 864 inside samples of the cases using the LUT, PCA and wPCA methods. The camera is the Nikon D5100. The insets show enlarged parts. In (**b**), all the counts in the "<0.99" slot have *GFC* < 0.99.

The computation time required for the LUT method is at least two orders of magnitude faster than that required for reconstruction methods using basis spectra that emphasize the relationship between the test and training samples [13]. In this work, the ratio of the computation time required to use the LUT method and wPCA method was 1:80.2, where samples were reconstructed from their signal vector C to the spectral reflectance vector S_{RefRec} using MATLAB on the Windows 10 platform.

5.2. Extrapolation Using the LUT Method Utilizing Optimized ARSs

The color filters optimized as in Section 4.2 were used to create the ARSs in this subsection. The edge wavelengths of the optimized color filters for the Nikon D5100 and CMF cameras are shown in Table 3. The filter spectral transmittance for the Nikon D5100 and CMF cameras is shown in Figure 7a,b, respectively. From Table 4, there were 202 and 203 outside samples for the Nikon D5100 and CMF cameras, respectively. The assessment metric statistics for the outside samples are shown in Table 4. As expected, the mean assessment metrics for the outside samples were worse than those for the inside samples. The assessment metric statistics for the two cameras were about the same except for the color difference ΔE_{00}. The assessment metric statistics for all samples are also shown in Table 4.

For the Nikon D5100, there were 98, 79, 22 and 3 outside samples that referenced 1, 2, 3 and 4 ARSs, respectively. Figure 12a–f show the reconstructed spectra S_{Rec} using the LUT method for the 2.5G 7/6, 10P 7/8, 2.5R 4/12, 2.5Y 9/4, 10BG 4/8 and 5PB 4/12 color chips, respectively, where their target spectrum $S_{Reflection}$ and neighboring reference spectra are also shown. The case in Figure 12a is an interpolation example for comparison. The cases in Figure 12b–f are extrapolation examples. For the cases in Figure 12b–f, the numbers of referenced ARSs are 1, 2, 2, 3 and 4, respectively. The ARS neighborhoods are indicated in the figures. Neighborhood 3 is the black ARS for the case in Figure 12e. The spectrum was well recovered for the case in Figure 12f, although four ARSs were referenced. The reconstructed spectral reflectance S_{RefRec} for the cases in Figure 12a–f is shown in Figure 13a–f, respectively. RMS errors $E_{Ref} = 0.004$, 0.0223, 0.014, 0.0165, 0.0159 and 0.0149 for the cases in Figure 13a–f, respectively.
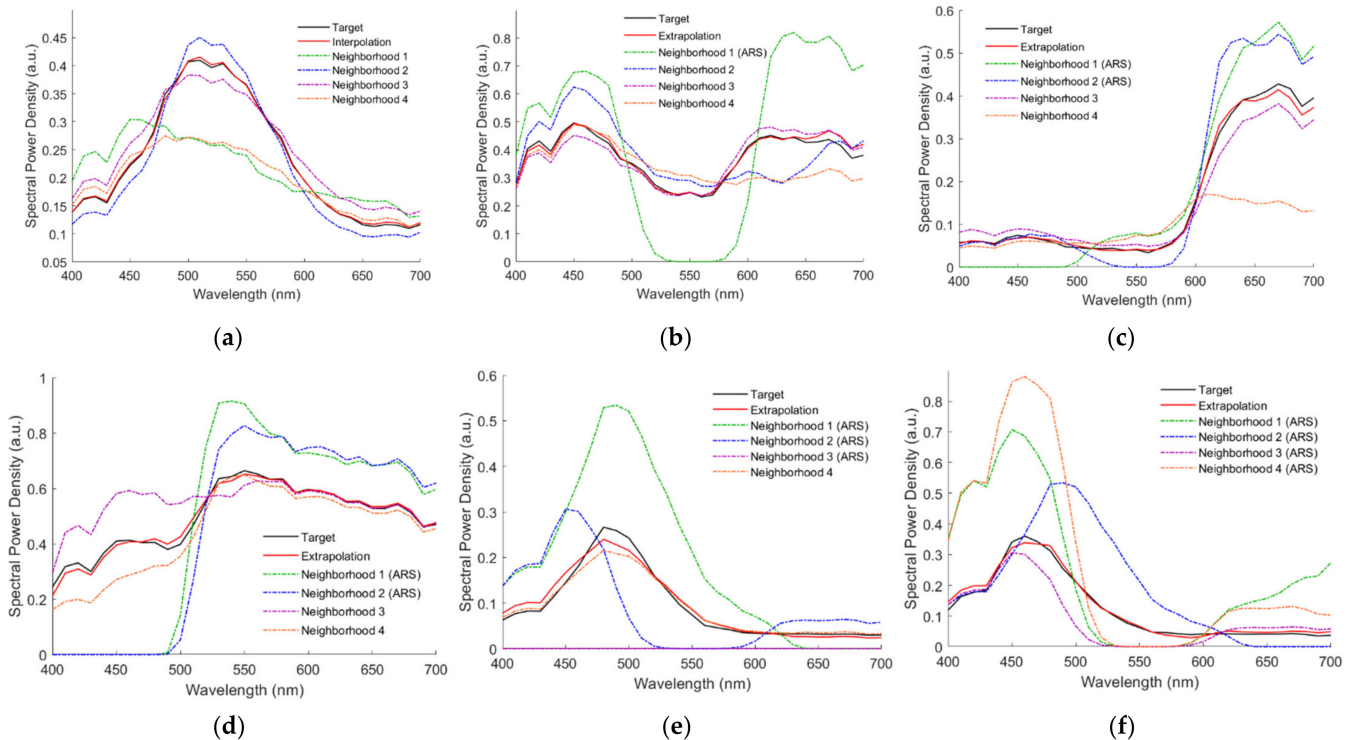

(a) (b) (c)

(d) (e) (f)

Figure 12. Target spectrum $S_{Reflection}$, reconstructed spectra S_{Rec} and neighboring reference spectra using the LUT method and optimized color filters. Munsell annotations of the color chips are (**a**) 2.5G 7/6, (**b**) 10P 7/8, (**c**) 2.5R 4/12, (**d**) 2.5Y 9/4, (**e**) 10BG 4/8 and (**f**) 5PB 4/12.

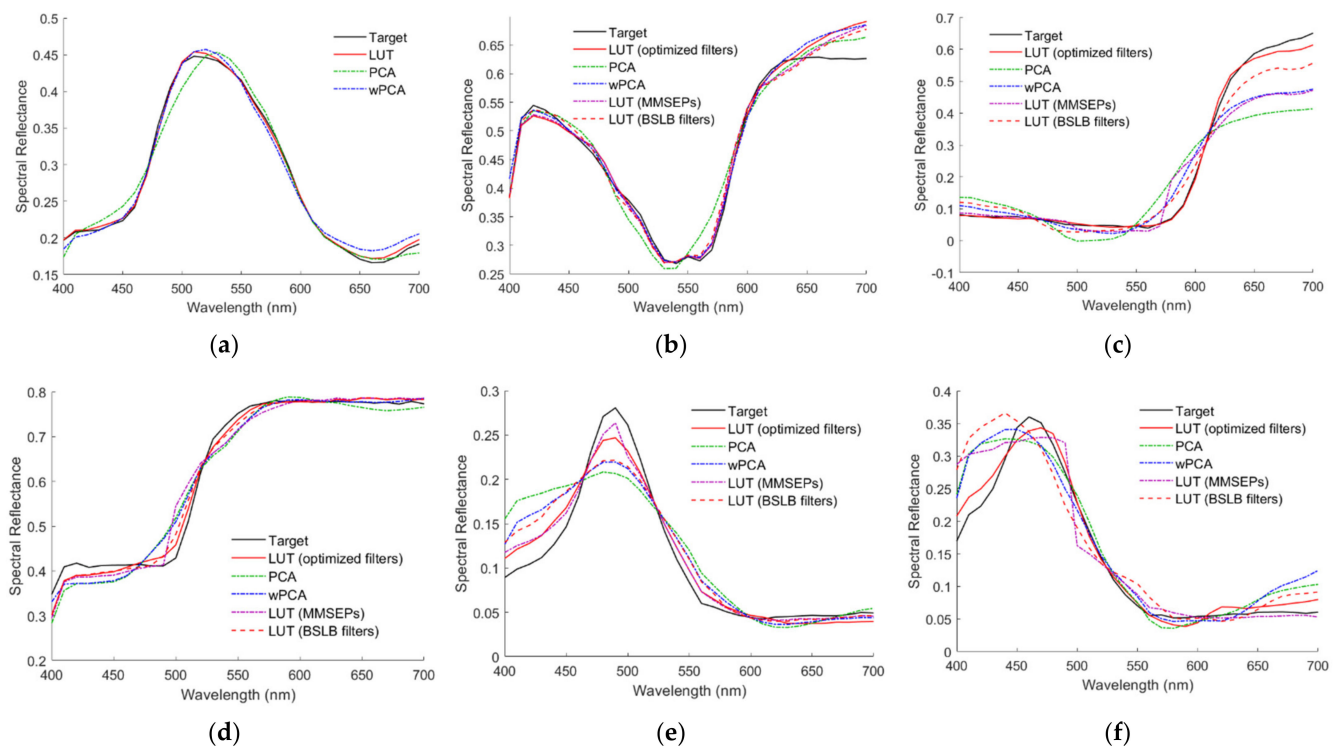**Figure 13.** (**a**–**f**) show the target spectral reflectance S_{Ref} and reconstructed spectral reflectance S_{RefRec} for the cases in Figure 12a–f, respectively. The results using the other reconstruction methods are also shown. Refer to Sections 5.1–5.4 for details.

5.3. Comparison of Extrapolations using Different Methods

5.3.1. PCA and wPCA Methods

Table 5 shows the assessment metric statistics for the 202 outside samples of the Nikon D5100 using the PCA and wPCA methods. As expected, the spectrum reconstruction error using the wPCA method was apparently smaller than that using the PCA method. Comparing Table 4 with Table 5, we can see that the extrapolation using the LUT method utilizing optimized ARSs outperformed the wPCA method. Note that the ratio of good fit *RGF99* was reduced from 0.9803 for the inside samples to 0.7772 for the outside samples when using the wPCA method, i.e., 22.28% of the outside samples had a *GFC* of less than 0.99. When using the LUT method utilizing optimized ARSs, *RGF99* was slightly reduced from 0.9375 for the inside samples to 0.9257 for the outside samples. It was found that when ARSs were included in the training samples of the wPCA method, the extrapolation error did not decrease, but increased further.

Figure 13a–f also show the reconstructed spectral reflectance using the PCA and wPCA methods. The RMS errors E_{Ref} = 0.0135, 0.0246, 0.1142, 0.0352, 0.0393 and 0.0366 for the cases using the PCA method in Figure 13a–f, respectively. The RMS errors E_{Ref} = 0.0095, 0.0221, 0.0794, 0.03, 0.0297 and 0.0392 for the cases using the wPCA method in Figure 13a–f, respectively.

5.3.2. Nearest Tetrahedron 3D Extrapolation Method

By definition, an outside sample cannot be enclosed by any tetrahedron in the tetrahedral mesh of reference samples in the RGB signal space. However, it can be extrapolated from the nearest tetrahedron [13]. The reference samples of the tetrahedron vertices are used to extrapolate the outside sample, using the same method as interpolation, except that the coefficients in Equation (1a,b) are not restricted to be between 0 and 1. The nearest tetrahedron can be located according to its circumcenter, in-center or centroid. For example, if the locating rule is based on the circumcenter, the nearest tetrahedron is the tetrahedron with the shortest Euclidian distance between its circumcenter and the outside sample.

Table 6 shows the assessment metric statistics for the 202 outside samples of the Nikon D5100 using the nearest tetrahedron 3D extrapolation method. The methods in the table using the locating rules based on the circumcenter, in-center and centroid are designated as NTCC, NTIC and NTCE, respectively. The results using the LUT method utilizing optimized ARSs and the wPCA method shown in Tables 4 and 5 are also shown in Table 6 for comparison. As can be seen from Table 6, the mean extrapolation error using the NTCC method was much less than that of the NTIC and NTCE methods but was larger than that of the LUT method utilizing optimized ARSs.

Table 6. Assessment metric statistics for the 202 outside samples of the Nikon D5100 using the NTCC method, NTIC method, NTCE method, LUT method utilizing MMSEP samples and LUT method utilizing ARSs in the BSLB case (ARS(BSLB)). Also shown are the cases using the LUT method utilizing optimized ARSs (ARS(Opt)) and the wPCA method for comparison.

Metric	Statistics	NTCC	NTIC	NTCE	MMSEP	ARS (BSLB)	ARS (Opt)	wPCA
E_{Ref}	mean μ	0.0258	0.0393	0.0470	0.0212	0.0190	0.0171	0.0213
	std σ	0.0225	0.0600	0.0712	0.0201	0.0164	0.0150	0.0194
	PC50	0.0196	0.0173	0.0193	0.0164	0.0154	0.0132	0.0155
	PC98	0.0967	0.2493	0.3295	0.0819	0.0728	0.0599	0.0774
	MAX	0.1279	0.4292	0.4292	0.1531	0.1003	0.1078	0.1255
GFC	mean μ	0.9856	0.9703	0.9617	0.9951	0.9948	0.9962	0.9931
	std σ	0.0313	0.0878	0.0981	0.0090	0.0093	0.0084	0.0118
	PC50	0.9971	0.9965	0.9961	0.9981	0.9982	0.9986	0.9976
	MIN	0.8355	0.3718	0.3718	0.9356	0.9376	0.9193	0.8921
	RGF99	0.7475	0.6931	0.6485	0.8812	0.8416	0.9257	0.7772
ΔE_{00}	mean μ	0.7198	1.0659	1.7758	0.5900	0.6847	0.4262	0.8011
	std σ	0.6564	1.6787	4.3453	0.5657	0.6437	0.3827	0.7887
	PC50	0.5217	0.5207	0.5629	0.3419	0.4782	0.3015	0.5094
	PC98	2.8621	6.8300	21.3735	2.1651	2.5164	1.6402	3.0850
	MAX	3.4551	15.3924	32.8994	2.8408	3.2615	1.8962	3.3029
SCI	mean μ	8.7137	12.5158	16.5762	6.9223	7.3756	5.6495	8.6050
	std σ	6.0169	16.4821	26.2679	5.5522	5.7411	3.7252	7.1555
	PC50	7.5725	7.1176	7.6722	5.7158	5.4641	4.6951	6.3268
	PC98	25.7363	61.6082	130.5460	23.4707	22.2341	15.0412	31.3431
	MAX	30.4515	135.4394	157.6624	38.2342	32.9033	21.9370	35.2093

5.3.3. LUT Method Utilizing MMSEP Samples

The extrapolation using the LUT method utilizing MMSEP samples is considered. As described in Section 1, eight spectral reflectance functions were constructed so that their color points under D65 illumination were as close as possible to the corners of the RGB signal cube. The eight MMSEP samples were included in the reference sample dataset for extrapolation. The white MMSEP sample and black MMSEP sample are the same as the white ARS and black ARS, respectively. The spectral reflectance functions of the other six MMSEPs are based on the sigmoid function with parameters optimized for the minimum objective function defined in [14].

Table 7 shows the optimized RGB signal values of the MMSEP samples for the Nikon D5100. The RGB signal values were not close to their target values, except for the white and black MMSEP samples. Taking the green MMSEP sample as an example, if the value of its G signal is close to 1.0, its R and B signals will not be small in value because the spectral sensitivities overlap, as shown in Figure 1a. The convex hull of the eight MMSEP samples is shown as a red mesh in Figure 10a,b. The convex hull H_{AR} is smaller in size than the MMSEP convex hull but extends more in the yellow and purple regions. The convex hull H_{AR} can be expanded further if red, green and blue filters are used. The LUT method utilizing MMSEP samples is equivalent to the LUT method utilizing only eight ARSs, where six color filters are used and the white card is the only reflective surface.

Table 7. Target and optimized RGB signal values of MMSEP samples for the Nikon D5100.

	Target			Optimized		
Signal	**R**	**G**	**B**	**R**	**G**	**B**
Red	1	0	0	0.8174	0.1221	0.008
Green	0	1	0	0.1874	0.6941	0.19
Blue	0	0	1	0.0736	0.2255	0.8014
Cyan	0	1	1	0.1771	0.8719	0.9863
Magenta	1	0	1	0.8506	0.3245	0.8051
Yellow	1	1	0	0.9261	0.7720	0.1972
White	1	1	1	1	1	1
Black	0	0	0	0	0	0

The assessment metric statistics for the 202 outside samples of the Nikon D5100 using the LUT method utilizing MMSEP samples are shown in Table 6. There were 148, 46 and 8 outside samples that referenced 1, 2 and 3 MMSEP samples, respectively. As can be seen from Table 6, using the optimized ARSs improved the assessment metrics compared to using MMSEP samples. Figure 13b–f also show the reconstructed spectral reflectance using the LUT method utilizing MMSEP samples, where the RMS errors E_{Ref} = 0.0198, 0.0846, 0.0331, 0.0148 and 0.038, respectively. For the cases in Figure 13b–f, the numbers of referenced MMSEP samples are 1, 3, 1, 2 and 1, respectively.

Figure 14a,b show the E_{Ref} and *GFC* histograms for the 202 outside samples, respectively, where the cases using the LUT method utilizing optimized ARSs, the wPCA method and the LUT method utilizing MMSEP samples are shown. For extrapolation, the LUT method utilizing optimized ARSs outperformed the wPCA method and the LUT method utilizing MMSEP samples.
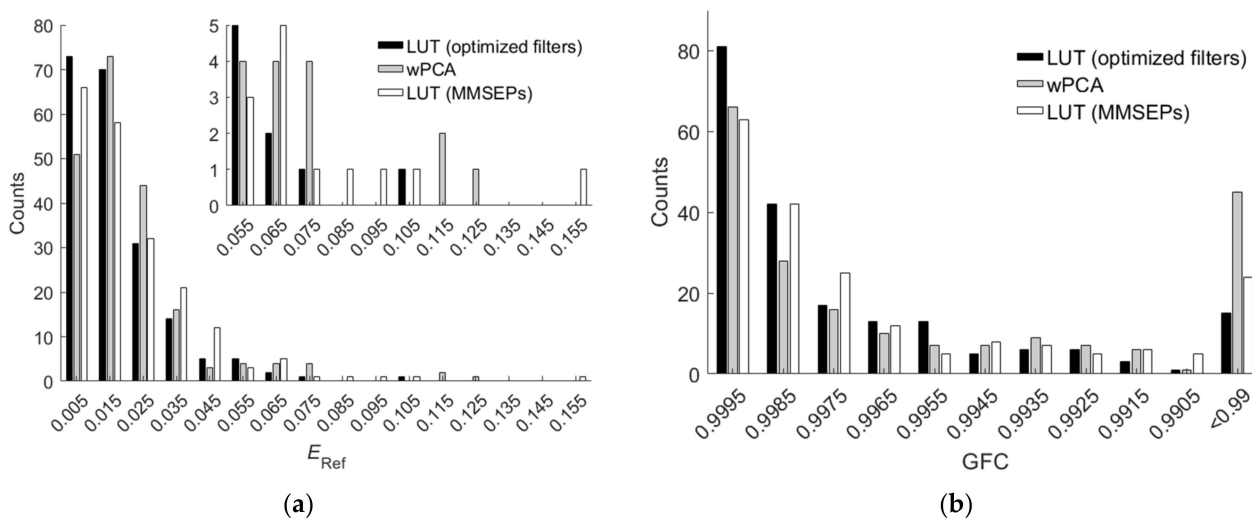

(**a**)   (**b**)

Figure 14. (**a**) E_{Ref} and (**b**) *GFC* histograms for the 202 outside samples of the cases using the LUT and wPCA methods. The results of the cases using the LUT method utilizing optimized ARSs and the LUT method utilizing MMSEP samples are shown. In (**a**), the inset shows an enlarged part. In (**b**), all the counts in the "<0.99" slot have *GFC* < 0.99.

5.4. Effect of Filter Edge Wavelengths

The spectral sensitivities of a camera can be measured or estimated as described in Section 1. If the measurements or estimates are accurate, the color filters can be optimized using the same method as in Section 4.2. On the other hand, estimates of sensitivity spectral shapes may not be very accurate, but estimates of channel wavelengths may be accurate enough for color filter design. It is found that the specifications of optimized color filters are related to the channel wavelengths. For the Nikon D5100, from Tables 2 and 3, the

optimized edge wavelengths λ_{Copt}, λ_{Yopt}, λ_{MSopt} and λ_{MLopt} are about $\lambda_{CamR} + \Delta\lambda_{CamR}/4$, $(\lambda_{CamC} + \lambda_{CamG})/2$, λ_{CamC} and λ_{CamR}, respectively, where λ_{CamC} is an average wavelength and

$$\lambda_{CamC} = (\lambda_{CamB} + \lambda_{CamG})/2, \tag{11}$$

These approximate relationships are roughly valid for the CMF camera. Since the channel wavelength is the average wavelength of the spectral sensitivity, the specifications of appropriate color filters could be estimated from less accurate estimates of the spectral sensitivities.

In this subsection, the use of color filters that are not optimized is studied. Deviations of filter specifications from their optimized values are expressed as $\delta\lambda_C = \lambda_C - \lambda_{Copt}$, $\delta\lambda_Y = \lambda_Y - \lambda_{Yopt}$, $\delta\lambda_{MS} = \lambda_{MS} - \lambda_{MSopt}$ and $\delta\lambda_{ML} = \lambda_{ML} - \lambda_{MLopt}$. It is found that the appropriate range of edge wavelengths can be roughly estimated as

$$\lambda_{CamY} \leq \lambda_C \leq \lambda_{Copt}, \tag{12a}$$

$$\lambda_{CamC} \leq \lambda_Y \leq \lambda_{Yopt}, \tag{12b}$$

$$\lambda_{CamB} \leq \lambda_{MS} \leq \lambda_{MSopt}, \tag{12c}$$

$$\lambda_{CamY} \leq \lambda_{ML} \leq \lambda_{MLopt}, \tag{12d}$$

where λ_{CamY} is an average wavelength and

$$\lambda_{CamY} = (\lambda_{CamG} + \lambda_{CamR})/2. \tag{13}$$

For the Nikon D5100, $\lambda_{CamC} = 498.7$ nm and $\lambda_{CamY} = 567$ nm. The empirical estimates shown in Equation (12a–d) are based on the comparison of Figure 7a,b with Figure 1a,b, respectively, and the tolerance analysis shown below.

The deviation of the edge wavelength from the optimized value results in a change in the convex hull H_{RA}. Since $\lambda_{Copt} > \lambda_{CamR}$, increasing positive $\delta\lambda_C$ will result in an increase in the *R* signal with little change in the *B* and *G* signals, which will cause the ratios *B/R* and *G/R* to decrease. The decrease in the signal saturation results in a smaller convex hull H_{RA} in the cyan region, and some outside samples may not be extrapolated. Therefore, the upper bound in Equation (12a) is set to the optimized edge wavelength of the cyan filter. The upper bounds in Equation (12b–d) are changed for similar reasons. Since $\lambda_{CamC} < \lambda_{Yopt} < \lambda_{CamG}$, increasing positive $\delta\lambda_Y$ will result in a greater reduction in the *G* signal, which will cause the ratio *G/B* to decrease. Since $\lambda_{MSopt} \approx \lambda_{CamC}$ and $\lambda_{MLopt} \approx \lambda_{CamR}$, increasing positive $\delta\lambda_{MS}$ and $\delta\lambda_{ML}$ will result in a greater increase in the *G* signal and a greater reduction in the *R* signal, respectively, which will cause the ratios *B/G* and *R/G* to decrease.

Figure 15a–i show the mean RMS error E_{Ref} of outside samples versus $\delta\lambda_{MS}$ and $\delta\lambda_{ML}$, where the values of $\delta\lambda_C$ and $\delta\lambda_Y$ are shown in the figures. The camera is the Nikon D5100. In the figures, $\delta\lambda_C = -51.9$ nm and -15.5 nm correspond to $\lambda_C = \lambda_{CamY}$ and λ_{CamR}, respectively; $\delta\lambda_Y = -12.1$ nm corresponds to $\lambda_Y = \lambda_{CamC}$. The white symbols "+" and "x" are the origin ($\delta\lambda_{MS} = \delta\lambda_{ML} = 0$ nm) and the point of the minimum mean E_{Ref} in each figure, respectively. The values of the mean E_{Ref} at the origin and at the point of the minimum mean E_{Ref} are shown in Tables 8 and 9, respectively, for the cases in Figure 15a–i. In the two tables, the corresponding filter edge wavelength deviations and the ratio *RGF99* are also shown.
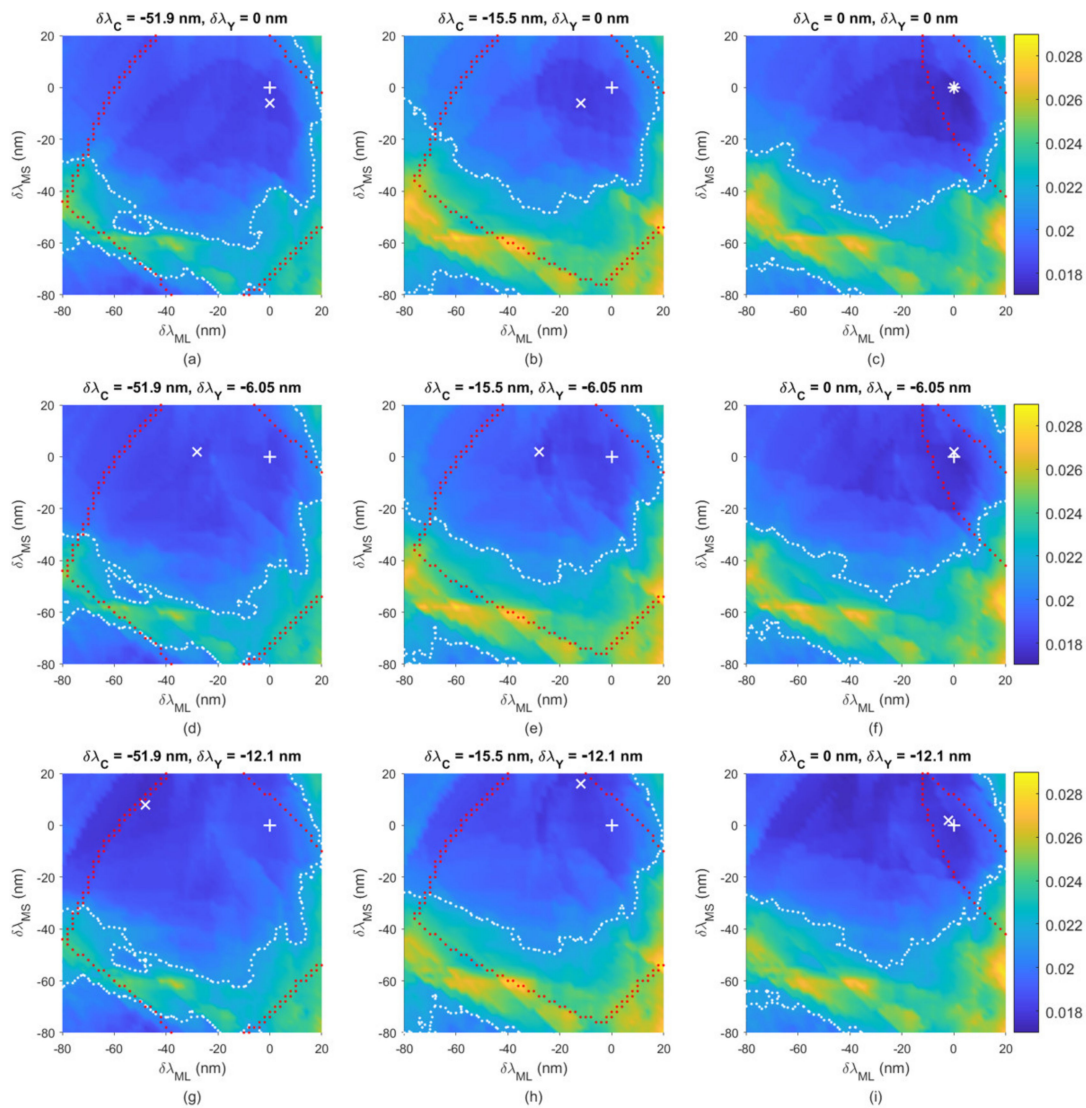
Figure 15. Mean E_{Ref} of 202 outside samples versus $\delta\lambda_M$ and $\delta\lambda_{Sep}$ for the Nikon D5100, where the values of $\delta\lambda_C$ and $\delta\lambda_Y$ are shown in (**a–i**). The white symbols "+" and "×" are the origin and the point of the minimum mean E_{Ref} in the figure, respectively. The red dotted line is the boundary where at least one outside sample cannot be extrapolated. Beyond the boundary, the mean E_{Ref} of outside samples that can be extrapolated is shown. The white dotted line is the contour of $E_{Ref} = 0.0213$.

Table 8. Filter edge wavelength deviations and the mean RMS error E_{Ref} of outside samples at the origin in Figure 15a–i. The ratio *RGF99* of outside samples is also shown.

Figure 15	$\delta\lambda_C$ (nm)	$\delta\lambda_Y$ (nm)	$\delta\lambda_{MS}$ (nm)	$\delta\lambda_{ML}$ (nm)	*Mean E_{Ref}*	*RGF99*
(**a**)	−51.9	0	0	0	0.0181	0.8614
(**b**)	−15.5	0	0	0	0.0182	0.8713
(**c**)	0	0	0	0	0.0171	0.9257
(**d**)	−51.9	−6.05	0	0	0.0182	0.8564
(**e**)	−15.5	−6.05	0	0	0.0183	0.8762
(**f**)	0	−6.05	0	0	0.0173	0.9208
(**g**)	−51.9	−12.1	0	0	0.0187	0.8614
(**h**)	−15.5	−12.1	0	0	0.0185	0.8812
(**i**)	0	−12.1	0	0	0.0176	0.9257

Table 9. The minimum mean RMS error E_{Ref} of outside samples in Figure 15a–i and corresponding filter edge wavelength deviations. The ratio *RGF99* of outside samples is also shown.

Figure 15	$\delta\lambda_C$ (nm)	$\delta\lambda_Y$ (nm)	$\delta\lambda_{MS}$ (nm)	$\delta\lambda_{ML}$ (nm)	*Mean E_{Ref}*	*RGF99*
(**a**)	−51.9	0	−6	0	0.018	0.8614
(**b**)	−15.5	0	−6	−12	0.0178	0.8911
(**c**)	0	0	0	0	0.0171	0.9257
(**d**)	−51.9	−6.05	2	−28	0.0181	0.8713
(**e**)	−15.5	−6.05	2	−28	0.0179	0.9109
(**f**)	0	−6.05	2	0	0.0173	0.9208
(**g**)	−51.9	−12.1	8	−48	0.0178	0.8663
(**h**)	−15.5	−12.1	16	−12	0.0177	0.9158
(**i**)	0	−12.1	2	−2	0.175	0.9307

At the origin in Figure 15a–i, all outside samples can be extrapolated. Away from the origin, the red dotted line represents the boundary where at least one outside sample cannot be extrapolated. Beyond the boundary, the mean E_{Ref} of outside samples that can be extrapolated is shown. The white dotted line in the figure represents the contour of the mean $E_{Ref} = 0.0213$, which is the value obtained using the wPCA method. Using color filters that meet the specifications within both the red and white dotted lines, all outside samples can be extrapolated while keeping the mean $E_{Ref} < 0.0213$. For the cases with $\delta\lambda_C = 0$ in Figure 15c,f,i, the area enclosed by the red and white dotted lines is small because some cyan outside samples cannot be extrapolated. They can be extrapolated by using a blue-shift cyan filter, i.e., $\delta\lambda_C < 0$, but will increase the extrapolation error. When $\delta\lambda_C = −9.0$ nm, the red dotted line is about the same as in the cases of $\delta\lambda_C = −15.5$ nm in Figure 15b,e,h. Therefore, if a larger edge wavelength tolerance is required, a blue-shift cyan filter is preferred. For such a requirement, the upper bound λ_{Copt} in Equation (12a) can be replaced by λ_{CamR}.

The point of $(\delta\lambda_{ML}, \delta\lambda_{MS}) = (−41.1$ nm, $−33$ nm$)$ in Figure 15g is the lower bound case in Equation (12a–d), where $\lambda_C = \lambda_{CamY}$, $\lambda_Y = \lambda_{CamC}$, $\lambda_{MS} = \lambda_{CamB}$ and $\lambda_{ML} = \lambda_{CamY}$. Since all filter edge wavelengths are blue-shifted, this case is called the blue-shift lower bound (BSLB) case. In contrast, the upper bound case in Equation (12a–d) is the optimized case at the origin in Figure 15c. The assessment metric statistics of the BSLB case are shown in Table 6, where the mean $E_{Ref} = 0.019$ and *RGF99* $= 0.8416$. As can be seen from Table 6, the assessment metric statistics of the BSLB case were worse than those of the optimized case, but better than those of the wPCA and NTCC methods. Figure 13b–f also show the reconstructed spectral reflectance of the BSLB case, where the RMS errors $E_{Ref} = 0.0187$, 0.0469, 0.0203, 0.0274 and 0.0482, respectively.

Figure 16a,b show the E_{Ref} and *GFC* histograms, respectively, for the 202 outside samples of the BSLB case. Also shown are the results of the cases using the LUT method utilizing optimized ARSs and the LUT method utilizing MMSEP samples for comparison. As can be seen from the two figures and Table 6, for the RMS error E_{Ref}, the unoptimized BSLB case was slightly better than the case including MMSEP samples, but for the goodness-of-fit coefficient *GFC*, the case including MMSEP samples was slightly better. The extrapolation performance of the two cases is comparable. Note that it is easy to design better color filters than the BSLB case for extrapolation.
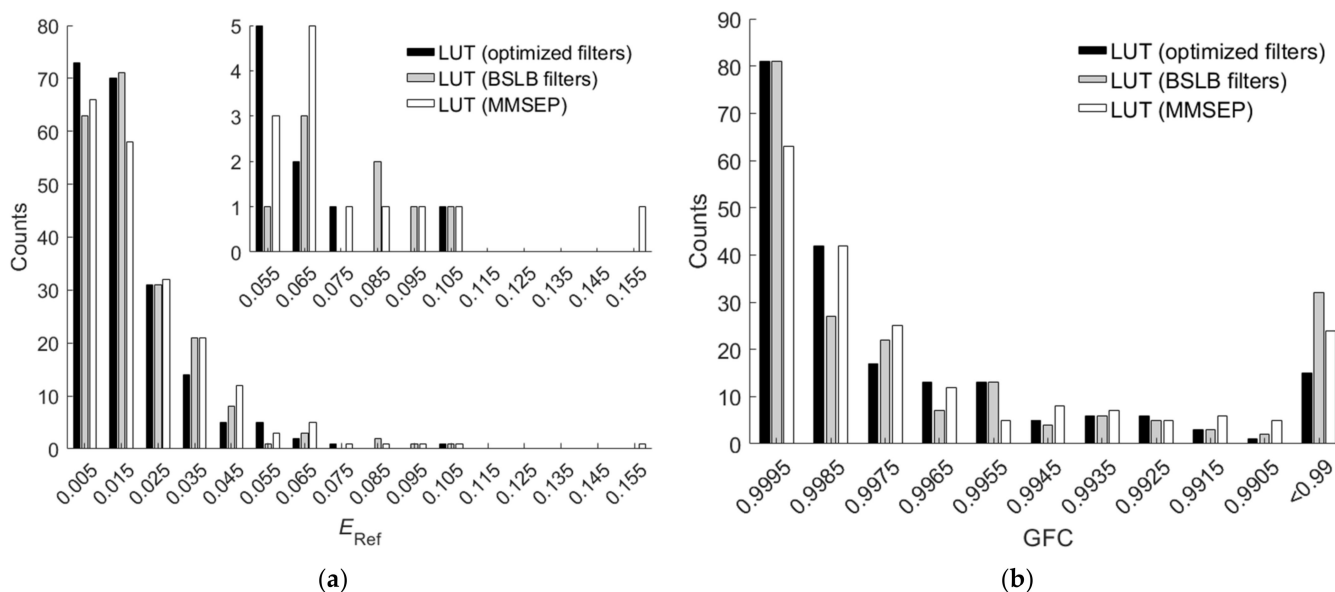
Figure 16. (**a**) E_{Ref} and (**b**) *GFC* histograms for the 202 outside samples of the BSLB case. Also shown are the results of the cases using the LUT method utilizing optimized ARSs and the LUT method utilizing MMSEP samples for comparison. In (**a**), the inset shows an enlarged part. In (**b**), all the counts in the "<0.99" slot have *GFC* < 0.99.

6. Conclusions

The reconstruction of spectral reflectance using the LUT method to interpolate camera RGB signals was investigated. Using the LUT method has the advantages of a high accuracy, saving computation time and eliminating the need to use the camera spectral sensitivity functions. The disadvantage of this method is that it cannot interpolate samples outside the convex hull of the reference samples in the RGB signal space. The outside samples can be extrapolated by using the method based on basis spectra, but it has two disadvantages: (1) accurate camera spectral sensitivity functions are required; (2) the calculation of the algorithm with a low spectrum reconstruction error is time-consuming. This paper proposed the LUT method utilizing auxiliary reference samples for extrapolating outside samples. The auxiliary reference samples were created by using reference samples and color filters so that the convex hull of the reference samples and auxiliary reference samples can enclose the outside samples in the RGB signal space. Therefore, outside samples can be extrapolated by using the LUT method utilizing auxiliary reference samples.

The proposed method was tested with Munsell color chips as examples of reflective surfaces. The Nikon D5100 camera was taken as an example camera. The method to create auxiliary reference samples was described. Cyan, yellow and magenta filters were used in this study. The optimized design of the three filters was presented. The results show that the mean extrapolation error using the proposed method was smaller than that of the weighted PCA method. The specifications for the optimized color filters mainly depend on the average wavelengths of the camera spectral sensitivities. The appropriate range of color filter edge wavelengths was shown. The design of color filters may not require accurate measurement or estimation of the camera spectral sensitivities. Therefore, the proposed method is feasible for overcoming the extrapolation problem. It was also shown that the ratio of computation time required to use the LUT method and the wPCA method was 1:80.2.

Since only one commercially available camera was considered, further studies are required for cameras with other sensitivity characteristics. Further research should use more than three color filters to expand the convex hull of the reference samples and auxiliary reference samples, and further reduce the extrapolation error where possible. Studies implementing the proposed method for field application will be published in the future.

References

1. Liang, H.; Saunders, D.; Cupitt, J. A new multispectral imaging system for examining paintings. *J. Imag. Sci. Technol.* **2005**, *49*, 551–562.
2. Liang, J.; Wan, X.; Liu, Q.; Li, C.; Li, J. Research on filter selection method for broadband spectral imaging system based on ancient murals. *Col. Res. Appl.* **2015**, *41*, 585–595. [CrossRef]
3. Kim, D.B.; Jang, I.Y.; Choi, H.K.; Lee, K.H. Recovery and representation of spectral bidirectional reflectance distribution function from an image-based measurement system. *Col. Res. Appl.* **2015**, *41*, 358–371. [CrossRef]
4. Schaepman, M.E. Imaging spectrometers. In *The SAGE Handbook of Remote Sensing*; Warner, T.A., Nellis, M.D., Foody, G.M., Eds.; Sage Publications: Los Angeles, CA, USA, 2009; pp. 166–178.
5. Cai, F.; Lu, W.; Shi, W.; He, S. A mobile device-based imaging spectrometer for environmental monitoring by attaching a lightweight small module to a commercial digital camera. *Sci. Rep.* **2017**, *7*, 15602. [CrossRef]
6. Zhao, Y.; Berns, R.S. Image-based spectral reflectance reconstruction using the matrix R method. *Col. Res. Appl.* **2007**, *32*, 343–351. [CrossRef]
7. Tzeng, D.Y.; Berns, R.S. A review of principal component analysis and its applications to color technology. *Col. Res. Appl.* **2005**, *30*, 84–98. [CrossRef]
8. Agahian, F.; Amirshahi, S.A.; Amirshahi, S.H. Reconstruction of reflectance spectra using weighted principal component analysis. *Col. Res. Appl.* **2008**, *33*, 360–371. [CrossRef]
9. Attarchi, N.; Amirshahi, S.H. Reconstruction of reflectance data by modification of Berns' Gaussian method. *Col. Res. Appl.* **2009**, *34*, 26–32. [CrossRef]
10. Hamza, A.B.; Brady, D.J. Reconstruction of reflectance spectra using robust nonnegative matrix factorization. *IEEE Trans. Signal Process.* **2006**, *54*, 3637–3642. [CrossRef]
11. Kim, B.G.; Han, J.; Park, S. Spectral reflectivity recovery from the tristimulus values using a hybrid method. *J. Opt. Soc. Am. A* **2012**, *29*, 2612–2621. [CrossRef]
12. Abed, F.M.; Amirshahi, S.H.; Abed, M.R.M. Reconstruction of reflectance data using an interpolation technique. *J. Opt. Soc. Am. A* **2009**, *26*, 613–624. [CrossRef]
13. Kim, B.G.; Werner, J.S.; Siminovitch, M.; Papamichael, K.; Han, J.; Park, S. Spectral reflectivity recovery from tristimulus values using 3D extrapolation with 3D interpolation. *J. Opt. Soc. Korea* **2014**, *18*, 507–516. [CrossRef]
14. Chou, T.-R.; Hsieh, C.-H.; Chen, E. Recovering spectral reflectance based on natural neighbor interpolation with model-based metameric spectra of extreme points. *Col. Res. Appl.* **2019**, *44*, 508–525. [CrossRef]
15. Darrodi, M.M.; Finlayson, G.; Goodman, T.; Mackiewicz, M. Reference data set for camera spectral sensitivity estimation. *J. Opt. Soc. Am. A* **2015**, *32*, 381–391. Available online: http://spectralestimation.wordpress.com/data/ (accessed on 27 June 2022). [CrossRef]
16. Finlayson, G.; Darrodi, M.M.; Mackiewicz, M. Rank-based camera spectral sensitivity estimation. *J. Opt. Soc. Am. A* **2016**, *33*, 589–599. [CrossRef]
17. Maloney, L.T. Evaluation of linear models of surface spectral reflectance with small numbers of parameters. *J. Opt. Soc. Am. A* **1986**, *3*, 1673–1683. [CrossRef]
18. Valero, E.M.; Nieves, J.L.; Nascimento, S.M.C.; Amano, K.; Foster, D.H. Recovering spectral data from natural scenes with an RGB digital camera and colored Filters. *Col. Res. Appl.* **2007**, *32*, 352–360. [CrossRef]
19. Babaei, V.; Amirshahi, S.H.; Agahian, F. Using weighted pseudo-inverse method for reconstruction of reflectance spectra and analyzing the dataset in terms of normality. *Col. Res. Appl.* **2011**, *36*, 295–305. [CrossRef]
20. Liang, J.; Wan, X. Optimized method for spectral reflectance reconstruction from camera responses. *Opt. Express* **2017**, *25*, 28273–28287. [CrossRef]
21. Xiao, G.; Wan, X.; Wang, L.; Liu, S. Reflectance spectra reconstruction from trichromatic camera based on kernel partial least square method. *Opt. Express* **2019**, *27*, 34921–34936. [CrossRef]
22. Wen, S. Color Management for Future Video Systems. *Proc. IEEE* **2013**, *101*, 31–44. [CrossRef]

23. Kohonen, O.; Parkkinen, J.; Jaaskelainen, T. Databases for spectral color science. *Col. Res. Appl.* **2006**, *31*, 381–390. Available online: https://sites.uef.fi/spectral/munsell-colors-matt-spectrofotometer-measured/ (accessed on 27 June 2022). [CrossRef]

24. Viggiano, J.A.S. A perception-referenced method for comparison of radiance ratio spectra and its application as an index of metamerism. *Proc. SPIE* **2002**, *4421*, 701–704.

25. Viggiano, J.A.S. Metrics for evaluating spectral matches: A quantitative comparison. In Proceedings of the International Conference on Computer Graphics, Imaging and Visualization, Penang, Malaysia, 26–29 July 2004; pp. 286–291.

26. Mansouri, A.; Sliwa, T.; Hardeberg, J.Y.; Voisin, Y. An adaptive-PCA algorithm for reflectance estimation from color images. In Proceedings of the 19th International Conference on Pattern Recognition, Tampa, FL, USA, 8–11 December 2008. [CrossRef]

27. Amidror, I. Scattered data interpolation methods for electronic imaging systems: A survey. *J. Electron. Imag.* **2002**, *11*, 157–176. [CrossRef]

28. Macleod, H.A. *Thin-Film Optical Filters*, 5th ed.; CRC Press: Boca Raton, FL, USA, 2018; Chapter 7.

29. Bayesian Optimization Algorithm. Available online: https://www.mathworks.com/help/stats/bayesian-optimization-algorithm.html (accessed on 27 June 2022).

30. Finlayson, G.D.; Mackiewicz, M.; Hurlbert, A. Color correction using root-polynomial regression. *IEEE Trans. Imag. Process.* **2015**, *24*, 1460–1470. [CrossRef]